Light absorption properties and potential sources of particulate brown carbon in the Pearl River Delta region of China

Zhujie Li[1,2], Haobo Tan[2,3]*, Jun Zheng[1]*, Li Liu[2,4], Yiming Qin[5], Nan Wang[2,3], Fei Li[2,3], Yongjie Li[6], Mingfu Cai[4], Yan Ma[1], and Chak K. Chan[5]

[1]Collaborative Innovation Center of Atmospheric Environment and Equipment Technology, Nanjing University of Information Science and Technology, Nanjing, China

[2]Key Laboratory of Regional Numerical Weather Prediction, Institute of Tropical and Marine Meteorology, China Meteorological Administration, Guangzhou, China

[3]Foshan Meteorological Service of Guangdong Province,Foshan, China

[4]Department of Atmospheric Science, Sun yat-sen University, Guangzhou, China

[5]School of Energy and Environment, City University of Hong Kong, Hong Kong, China

[6]Department of Civil and Environmental Engineering, Faculty of Science and Technology, University of Macau, Macau, China

Correspondence to: Haobo Tan (hbtan@gd121.cn) and Jun Zheng (zheng.jun@nuist.edu.cn)

Abstract:

Brown carbon (BrC) is a special type of organic aerosols (OA), capable of absorbing solar radiation from near-ultraviolet (UV) to visible wavelengths, which may lead to an increased aerosol radiative effect in the atmosphere. While high concentrations of OAs have been observed in the Pearl River Delta (PRD) region of China, the optical properties and corresponding radiative forcing of BrC in the PRD are still not well understood. In this work, we conducted a set of comprehensive measurements of atmospheric particulate matter from 29 November 2014 to 2 January 2015 to investigate aerosol compositions, optical properties, source origins and radiative forcing effects at a suburban station in Guangzhou. The particle absorption Ångström exponent (AAE) was deduced and utilized to differentiate light absorption by BrC from that by black carbon (BC). The results showed that the average absorption contributions of BrC were 34.1±8.0% at 370 nm, 23.7±7.3% at 470 nm, 16.0±6.7% at 520 nm, 13.0±5.4% at 590 nm and 8.7±4.3% at 660 nm. A sensitivity analysis of the evaluation of the absorption Ångström exponent of BC (AAE_{BC}) was conducted based on the Mie theory calculation assuming that the BC-containing aerosol was mixed with the core-shell and external configurations. The corresponding uncertainty in AAE_{BC} was acquired. We found that variations in the imaginary refractive index (RI) of the BC core can significantly affect the estimation of AAE_{BC}. However, AAE_{BC} was relatively less sensitive to the real part of the RI of the BC core and was least sensitive to the real part of the RI of the nonlight absorbing shell. BrC absorption was closely related to aerosol potassium cation content (K^+), a common tracer of biomass burning emissions, which was most likely associated with straw burning in the rural area of the western PRD. Diurnal variation in BrC absorption revealed that primary organic aerosols had a larger BrC absorption capacity than secondary organic aerosols (SOAs). Radiative transfer simulations showed that BrC absorption may cause 2.3±1.8 W m^{-2} radiative forcing at the top of the atmosphere (TOA) and contribute to 15.8±4.4% of the aerosol warming effect. A chart was constructed to conveniently assess the BrC radiative forcing efficiency in the studied area with reference to certain aerosol single-scattering albedo (*SSA*) and BrC absorption contributions at various wavelengths. Evidently, the BrC radiative forcing efficiency was higher at shorter wavelengths.

Keywords: Brown carbon, Black carbon, Absorption Ångström exponent, Radiative forcing, Pearl River Delta.

48 **1 Introduction**

49 Black carbon (BC) and organic carbon (OC) are dominant carbonaceous aerosol components

50 that mainly originate from biomass burning in a global scale (Bond et al., 2004) and have

51 attracted great environmental concerns in rapidly developing regions. Carbonaceous aerosols

52 can not only exert adverse impacts on public health, similar to other particulate matters, but

53 also significantly affect the terrestrial radiation balance with enormous uncertainties. In

54 previous studies, BC was often considered to be the only light-absorbing species (Andreae and

55 Gelencser, 2006), and OC was believed to only be able to scatter light, i.e., causing a cooling

56 effect (Bond et al., 2011). Nevertheless, it has been reported that some fraction of organic

57 aerosols (OAs) may also specifically contribute to light absorption from the near-ultraviolet

58 (UV) to visible wavelength range, which is referred to as brown carbon (BrC) (Kirchstetter et

59 al., 2004). BrC optical properties are strongly affected by its chemical composition and physical

60 structure, which are related to different BrC sources. BrC can originate not only from direct

61 emissions, including smoldering, biomass burning or any type of incomplete fuel combustion

62 process (Cheng et al., 2011; T. C. Bond et al., 1999), but also from secondary organic aerosol

63 formation processes, such as aqueous phase reactions in acidic solutions (Desyaterik et al., 2013)

64 or volatile organic compound (VOC) oxidation (Laskin et al., 2015; Sareen et al., 2010). In

65 addition, BrC could have a complicated molecular composition and intermix with other

66 substances, such as BC, non-absorbing OAs and other inorganic materials, making it

67 complicated to investigate BrC optical properties.

68 BC absorption is commonly assumed to be covering the full wavelength-range. However, the

69 light absorption property of BrC is believed to be more wavelength-dependent, which can be

70 represented by distinct absorption Ångström exponent (AAE) values, i.e., the power exponent

71 of the light absorption coefficient. A typical threshold for the AAE of BC (AAE_{BC}) of 1.6 has

72 been recommended to distinguish BrC from BC (Lack and Cappa, 2010), and the AAE of BrC

73 has been reported as having a wider range (2 to 7) (Hoffer et al., 2005). Based on the difference

74 in the wavelength dependence of light absorption between BC and BrC, previous studies have

75 applied the AAE method to differentiate light absorption by BrC through multiwavelength

76 optical measuring apparatus, such as 3-wavelength Photoacoustic Soot Spectrometer (PASS-3)

77 (Lack and Langridge, 2013), multiwavelength Aethalometer (Olson et al., 2015), etc. Based on

78 the AAE method, the BrC absorption contribution has been estimated to be approximately 6 to

79 41% of total aerosol light absorption at short wavelengths, e.g., at 370 nm and 405 nm

80 (Washenfelder et al., 2015). A uniform AAE_{BC} from ~300 nm up to ~700 nm (Moosmüller et

81 al., 2011) is commonly used when evaluating the BrC absorption contribution using the AAE

82 method. However, it has been reported that the AAE_{BC} can be influenced by the mixing state,

83 BC core size and morphology (Lack and Cappa, 2010). The lensing effect of the coating shell

84 may enhance BC light absorption, the magnitude of which may also depend on wavelength and

85 can alter the value of AAE_{BC} (Liu et al., 2018). Moreover, different values of AAE_{BC} have been

86 found in the near-infrared and UV ranges (Wang et al., 2018). Therefore, using the default value

87 of $AAE_{BC} = 1$ may lead to uncertainty in BrC absorption coefficient estimation.

88 Quantifying BrC optical absorption accurately is essential to interpret aerosol optical depth

89 (AOD), and the corresponding aerosol direct radiative forcing (DRF) on the atmosphere can

90 also be evaluated if the single-scattering albedo (*SSA*) and extinction coefficient of aerosols are

91 known. The estimation of the DRF of BrC has shown a distinct seasonal variation, indicating

92 the influence of different absorption properties of BrC (Arola et al., 2015). A global simulation

93 study indicated that the average warming effect at the TOA caused by BrC absorption can be

94 up to 0.11 W m^{-2}, corresponding to ~25% of that predicted from BC absorption only (Feng et

95 al., 2013).

96 During the last three decades, rapid economic development has led to severe air pollution

97 problems in the PRD region (Chan and Yao, 2008). With rapid increases in the automobile

98 population and factories, high loadings of SOAs have often been observed (Tan et al., 2016b).

99 Biofuel usage may also play a significant role during wintertime air pollution events in the PRD,

100 indicating that the contribution from BrC light absorption cannot be ignored (Wu et al., 2018).

101 Recently, BrC light absorption has been quantified by Qin et al. (2018) using the AAE method

102 in the PRD region. OA chemical composition was simultaneously measured by a high-

103 resolution time-of-flight aerosol mass spectrometer, and it was found that organic aerosols

104 originating from biomass burning possessed the most intense absorption capability and were

largely responsible for BrC absorption. Qin et al. (2018) also suggested that correlations between OA chemical compositions and BrC absorption were wavelength-dependent.

In this paper, we applied the homologous AAE differentiation method to quantify the fraction of aerosol light absorption by BrC using the measurements from a seven-wavelength Aethalometer. The potential error incurred with this methodology was determined using Mie theory simulations, especially for various complex refractive indexes of the BC core and the coating material. The correlation between BrC light absorption and water-soluble ions, which is used as the source tracer, was employed to identify potential BrC sources. An atmospheric radiative transfer model has also been applied to evaluate the impact of BrC on direct radiative forcing using surface-based aerosol optical properties and satellite-based surface-albedo data. The magnitudes of aerosol radiative forcing at the top of the atmosphere due to BC and BrC were also individually quantified.

2 Methodology

2.1 Sampling site

Field observations were conducted at the Panyu station (113°21′E, 23°00′N), which is a monitoring site of the Chinese Meteorological Administration (CMA) Atmospheric Watch Network (CAWNET) that is located on the summit of Dazhengang Mountain (approximately 150 m above sea level) in Guangzhou, China. Figure 1 shows the location of the Panyu site, which is situated at the center of the PRD and is separated from residential areas by at least 500 m. Some agricultural fields can be found to the west of the site. Although there were no significant pollution sources nearby, this suburban site was strongly affected by pollutants transported from the urban area of Guangzhou and crop residual fires transported from the rural area of the PRD. The field campaign was conducted from 29 November 2014 to 2 January 2015. During the measurement period, aerosol light scattering and extinction, BC concentration, particle number size distribution (PNSD), OC concentration, and the water-soluble ion concentrations of $PM_{2.5}$ were continuously monitored.

2.2 Measurements and data analysis

All instruments were housed inside the 2nd floor measurement room of a ~5-m tall, 2-story building. The ambient sample was taken on the roof by a 2-m long, 12.7-mm OD stainless steel inlet, and a $PM_{2.5}$ cyclone sampler was also used. The metal tubing was thermally insulated and

135   maintained at a constant temperature of ~25°C. A diffusion drier was also used in-line to dry

136   the relative humidity (RH) of the air sample below 30% before further analysis.

137   **2.2.1 Measurements of relevant species**

138   A TSI-3936 scanning mobility particle sizer (SMPS) and a TSI-3321 aerodynamic particle sizer

139   (APS) were utilized to measure the 10 to 500 nm mobility diameter and 0.5 to 2.5 μm

140   aerodynamic diameter of the PNSD, respectively. The aerodynamic diameters of the APS data

141   were converted into mobility diameters using a material density of 1.7 g cm^{-3}. A detailed data

142   merging method has been described by Cheng et al. (2006). Furthermore, the pipe diffusion

143   loss of SMPS has been corrected using the empirical formula proposed by Kulkarni et al. (1996).

144   An AE-33 Aethalometer (Magee Scientific Inc.) was utilized for BC mass concentration

145   measurement, which was derived from optical attenuation using a mass absorption cross section

146   (MAC) of 7.77 m^2 g^{-1} at 880 nm. The sensitivity of AE-33 was approximately 0.03 μg m^{-3} for

147   a 1-min time resolution and a 5.0 liter per minute (LPM) sample flow rate.

148   The PM$_{2.5}$ mass concentration was measured by an Environment Dust Monitor (Model

149   EDM180, GRIMM Inc.), which monitored the mass concentration of PM$_{2.5}$ and PM$_{10}$

150   simultaneously.

151   Water-soluble ions (potassium (K$^+$), calcium (Ca^{2+}), magnesium (Mg^{2+}), chloride (Cl$^-$), sulfate

152   (SO$_4^{2-}$), nitrate (NO$_3^-$), and ammonium (NH$_4^+$)) were measured with the Monitor for AeRosols

153   and Gases in Air (MARGA) (Model ADI2080, Metrohm Inc.), which is an online analyzer for

154   semi-continuous measurements of gases and water-soluble ions in aerosols (Li et al., 2010).

155   The MARGA was automatically calibrated with standard internal solutions during field

156   measurement. The MARGA utilized its own PM$_{2.5}$ sampling system provided by the

157   manufacturer.

158   The OC mass concentration was measured by a Sunset online OC/EC analyzer (Model RT-4)

159   with a laser transmittance-based charring correction (Wu et al., 2018; Wu et al., 2019). The

160   sample flow rate of the OC/EC analyzer was maintained at 8 LPM. For each measurement cycle

161   (one hour), samples were collected onto a quartz filter within the first 45 min and then thermal-

162   optically analyzed during the remaining 15 min. First, OC was completely volatized in oxygen-

163   free helium with a stepwise ramped temperature (600 °C and 840 °C). In the second stage, the

164   temperature was reduced to 550 °C, and then EC and pyrolyzed carbon (PC) were combusted

165 in an oxidizing atmosphere (10% oxygen in helium), while the temperature was increased up

166 to 870 °C step by step. The CO_2 converted from all of the carbon components was then

167 quantified by a nondispersive infrared absorption CO_2 sensor (Lin et al., 2009). An internal

168 calibration peak made by 5% methane in helium was applied to quantify OC and EC. To correct

169 the PC converted from OC to EC, a tunable pulsed diode laser beam was used to monitor the

170 laser transmittance through the quartz filter throughout the thermal-optical analysis (Bauer et

171 al., 2012).

172 **2.2.2 Measurements of optical properties**

173 Light extinction by aerosols at 532 nm was detected using a cavity ring-down aerosol extinction

174 spectrometer (CRDS) (Model XG-1000, Hexin Inc.) by measuring the decay times of laser

175 intensity through the aerosol-containing sample and the filtered background air sample under

176 the same conditions. The extinction coefficient (σ_{ext}) was calculated using the procedure

177 described by Khalizov et al. (2009).

178 Aerosol total scattering (σ_{sp}) was measured by a TSI-3563 integrated nephelometer at three

179 wavelengths (i.e., 450 nm, 550 nm, and 700 nm) and was calibrated with CO_2 following the

180 manual instructions. Particle free air was used to check the nephelometer background signal

181 once every two hours. The scattering coefficients at other wavelengths were extrapolated using

182 the following equations:

183
$$SAE = -\frac{ln\left(\sigma_{scat,\lambda_0}\right) - ln\left(\sigma_{scat,550nm}\right)}{ln(\lambda_0) - ln(550)} \tag{1}$$

184
$$\sigma_{scat}(\lambda) = \sigma_{scat}(550) \cdot \left(\frac{\lambda}{550}\right)^{-SAE} \tag{2}$$

185 where λ_0=450 nm is for wavelengths less than 550 nm and λ_0=700 nm is for wavelengths greater

186 than 550 nm. The corresponding time series of extinction coefficients, scattering coefficients,

187 and SSA at 532 nm was displayed in Fig. S1.

188 The Aethalometer was also used for multi-wavelength light absorption measurements in this

189 study. The seven-wavelength aerosol light attenuation coefficients (σ_{ATN}) were converted into

190 aerosol light absorption coefficients (σ_{abs}) using Eq. (3) (Coen et al., 2010), where k is the

191 parameter that accounts for the loading effect, ATN is the light attenuation through the filter

192 with sample loading and C_{ref} is a fixed multiple scattering parameter.

193
$$\sigma_{abs} = \frac{\sigma_{ATN}}{(1 - k \cdot ATN) \cdot C_{ref}} \tag{3}$$

194   The real-time k value was retrieved using the dual-spot loading correction algorithm developed

195   by Drinovec et al. (2015). The detailed formula of ATN can also be found in Drinovec et al.

196   (2015). C_{ref} is considered a constant that strongly depends on the filter matrix effect. However,

197   some studies have suggested that C_{ref} may vary with wavelength (Arnott et al., 2005; Segura et al.,

198   2014). For internal combustion engines and biomass burning, C_{ref} at 370 nm was expected to be

199   approximately 12% and 18% less than C_{ref} at 532 nm for the aerosol component, respectively

200   (Schmid et al., 2006). Different ambient observations also showed that C_{ref} may have regional

201   specificity, even though it was retrieved by the same methodology (Coen et al., 2010). In this

202   study, C_{ref} =3.29 was used in Eq. (3) at each wavelength, and this value was derived from the

203   slope of σ_{ATN} measured by the Aethalometer vs. σ_{abs}, which was deduced from the CRDS and

204   nephelometer measurements. This C_{ref} was also very similar to the C_{ref} of 3.48 determined from

205   an inter-comparison study between an Aethalometer and a photoacoustic soot spectrometer

206   during a field campaign conducted in the PRD region in 2004 (Wu et al., 2009).

207   The BC light absorption at certain wavelengths was derived from the absorption coefficient σ_{abs}

208   according to Beer-Lambert's law, and its variation between different pairs of wavelengths (i.e.,

209     $\sigma_{abs,BC,\lambda}$) is denoted by the absorption Ångström exponent (AAE) equation developed by

210   Ångström (1929):

211 $$\sigma_{abs,BC,\lambda} = \sigma_{abs,BC,\lambda_0} \times (\lambda_0/\lambda)^{AAE_{BC}} \tag{4}$$

212   It has been suggested that the AAE of BC may vary between short and long wavelength ranges

213   (Lack and Cappa, 2010); hence, applying a wavelength-independent AAE_{BC} may lead to

214   uncertainties in the BC absorption calculation from one wavelength to another. In this work,

215   the light absorptions of BC at various wavelengths were retrieved by a modified wavelength-

216   dependent AAE differentiation method conducted by Wang et al. (2018):

217 $$\sigma_{abs,BC,\lambda_1} = \sigma_{abs,BC,880nm} \times \left(\frac{880}{\lambda_1}\right)^{AAE_{BC,520\text{-}880nm}} \tag{5.1}$$

218 $$\sigma_{abs,BC,\lambda_2} = \sigma_{abs,BC,880nm} \times \left(\frac{880}{520}\right)^{AAE_{BC,520\text{-}880nm}} \times \left(\frac{520}{\lambda_2}\right)^{AAE_{BC,370\text{-}520nm}} \tag{5.2}$$

219   Here, $\sigma_{abs,BC,\lambda_1}$ represents the absorption coefficient due to only BC greater than 520 nm, and

220     $\sigma_{abs,BC,\lambda_2}$ represents the absorption coefficient of BC less than 520 nm. $AAE_{BC,\lambda_i\text{-}\lambda_{i+1}}$ (i=1, 2

221   and 3) represents the AAE of BC between a longer and shorter wavelength at λ_i=880, 520 and

222   370 nm and was calculated as:

$$AAE_{BC,\lambda_i-\lambda_{i+1}} = -\frac{ln(\sigma_{abs,BC,\lambda_i}) - ln(\sigma_{abs,BC,\lambda_{i+1}})}{ln(\lambda_i) - ln(\lambda_{i+1})} \qquad (6)$$

Accordingly, BrC absorption at a certain wavelength λ ($\sigma_{abs,BrC,\lambda}$) was equal to the value of total aerosol absorption ($\sigma_{abs,\lambda}$) minus BC absorption ($\sigma_{abs,BC,\lambda}$):

$$\sigma_{abs,BrC,\lambda} = \sigma_{abs,\lambda} - \sigma_{abs,BC,\lambda} \qquad (7)$$

The light absorption data at 880 nm ($\sigma_{abs,880nm}$) were selected to represent BC absorption ($\sigma_{abs,BC,880nm}$), which shall not be affected by BrC (Drinovec et al., 2015). It has been reported that the dust-related contributions of PM$_{2.5}$ were normally less than 5% in wintertime in Guangzhou; therefore, the influence from dust could be negligible in this study (Huang et al., 2014).

2.2.3 Estimation of AAE$_{BC}$

Traditionally, AAE$_{BC}$ was believed to be close to 1.0 (Bodhaine, 1995), which has been commonly used for BC measurements (Olson et al., 2015). However, studies have demonstrated that AAE$_{BC}$ can be affected by the refractive index of coating materials, mixing state, morphology, and BC core size (Liu et al., 2015). Therefore, using the default AAE$_{BC}$ = 1 may lead to uncertainty in BrC absorption estimation. To obtain the correct AAE$_{BC}$, a series of Mie theory calculations were conducted using a simplified core-shell model (Bohren and Huffman, 1983; Wang et al., 2018). We used a modified BHCOAT code and BHMIE code to calculate the aerosol optical properties of the core-shell and external mixture at different wavelengths (Cheng et al., 2006). In the Mie theory, a particle is taken as a perfect homogeneous sphere, and its extinction and scattering efficiencies, $Q_{ext,Mie,\lambda}$ and $Q_{scat,Mie,\lambda}$, respectively, are expressed as (Mie, 1908; Seinfeld and Pandis, 1998):

$$Q_{ext,Mie,\lambda} = \frac{2}{\alpha^2}\sum_{n=1}^{\infty}[(2n+1)Re(a_n + b_n)] \qquad (8)$$

$$Q_{scat,Mie,\lambda} = \frac{2}{\alpha^2}\sum_{n=1}^{\infty}[(2n+1)(|a_n|^2 + |b_n|^2)] \qquad (9)$$

where $\alpha = \pi D_p/\lambda$ is the size parameter; a_n and b_n are functions of the complex refractive index (RI) and α in the Riccati-Bessel form, respectively. *Re* in Eq. (8) denotes that only the real part of RI is taken. The absorption efficiency ($Q_{abs,Mie,\lambda}$) is thus the difference between the extinction and scattering efficiencies:

$$Q_{abs,Mie,\lambda} = Q_{ext,Mie,\lambda} - Q_{scat,Mie,\lambda} \qquad (10)$$

Then, the absorption coefficient $\sigma_{abs,Mie,\lambda}$ was obtained by the following (Bricaud and Morel, 1986):

$$\sigma_{abs,Mie,\lambda} = \int Q_{abs,Mie,\lambda} \cdot (\tfrac{\pi}{4} D_p^2) \cdot N(\log D_p) \cdot d \log D_p \qquad (11)$$

where $N(\log D_p)$ is the PNSD function. A two-component parameterization of dry particles, i.e., the BC core and the nonlight-absorbing species, was applied to calculate aerosol optical properties here (Wex et al., 2002). $\widetilde{m}_{core}$ represents the RI of the BC core, and $\widetilde{m}_{non}$ represents the RI of nonlight-absorbing particles.

In a realistic atmosphere, some nonlight-absorbing particles may exist independently without BC (Liu et al., 2013; Cheung et al., 2016). In this work, the portion of nonlight-absorbing particles at a certain size (D_p) was determined by our previous measurements at the same site using a Volatility Tandem Differential Mobility Analyzer (V-TDMA), during which completely vaporized (CV) particles at 300°C were referred to as nonlight-absorbing particles that externally mixed with other BC-containing particles. Thus, the PNSD of CV particles ($N(logD_p)_{CV}$) and BC-containing particles ($N(logD_p)_{BC}$) can be given by the following equations:

$$N(logD_p)_{CV} = N(logD_p)_{measure} \cdot \Phi(D_p)_{N,CV} \qquad (12)$$

$$N(logD_p)_{BC} = N(logD_p)_{measure} \cdot (1 - \Phi(D_p)_{N,CV}) \qquad (13)$$

where $N(logD_p)_{measure}$ is the PNSD of the measured particles from SMPS and APS. $\Phi(D_p)_{N,CV}$ was the number fraction of CV particles in different size bin.

A previous study applied three kinds of BC mixture models to calculate the aerosol optical properties, including external, homogenously internal and core-shell mixtures (Bohren and Huffman, 2007; Seinfeld and Pandis, 1998). To quantify the mixing state of BC, r_{ext} was defined as the mass fraction of externally mixed BC (M_{ext}) in total BC (M_{BC}):

$$r_{ext} = \frac{M_{ext}}{M_{BC}} \qquad (14)$$

Tan et al. (2016) suggested that two extreme conditions of external and core-shell mixtures comprised the actual mixing state of BC in the PRD. Hence, we simply divided the PNSD of BC into the PNSD from an external mixture of BC and a core-shell mixture of BC. The PNSDs

278 of externally mixed BC particles and core-shell mixed BC particles were referred to by the

279 following equations with a given r_{ext}.

$$N(logD_p)_{ext} = N(logD_p)_{BC} \cdot f_{BC} \cdot r_{ext} \tag{15}$$

$$N(logD_p)_{core-shell} = N(logD_p)_{BC} \cdot (1 - f_{BC} \cdot r_{ext}) \tag{16}$$

282 f_{BC} was defined as the BC volume fraction in the BC-containing particle volume, which can be

283 converted from the BC mass concentration:

$$f_{BC} = \frac{M_{BC}}{\rho_{BC} \cdot \Sigma_{D_P} N(logD_p)_{BC} \cdot (\frac{\pi}{6} \cdot D_p^3)} \tag{17}$$

285 where ρ_{BC} is the density of BC and is assumed to be 1.5 g cm^{-3} (Ma et al., 2012); M_{BC} is the BC

286 mass concentration derived from the multi-angle absorption photometer (MAAP), which was

287 obtained by an empirical formula from the Aethalometer that measured the BC concentration

288 ($M_{BC,AE}$), as proposed by Wu et al. (2009):

$$M_{BC} = 0.897 \cdot M_{BC, AE} - 0.062 \tag{18}$$

290 The PNSDs of externally mixed nonlight-absorbing particles and externally mixed BC particles

291 were input into the BHMIE code, and the PNSD of the core-shell mixed particles was imported

292 into the BHCOAT code. Another critical parameter for the core-shell model was the diameter

293 of the BC core. For the simplified core-shell model we applied, the visualization was that a

294 homogeneous BC core sphere was encapsulated in a shell of non-absorbing coating (Bohren

295 and Huffman, 2007). Without size-resolved coating thickness measurements, core-shell mixed

296 particles simply assumed that cores with the same diameter had the same coating thickness.

297 Therefore, the diameter of the BC core was calculated as follows:

$$D_{core} = D_p \cdot (\frac{f_{BC} - f_{BC} \cdot r_{ext}}{1 - f_{BC} \cdot r_{ext}})^{\frac{1}{3}} \tag{19}$$

299 D_{core} and D_p are inputted as parameters into a_n and b_n, respectively, which was described by

300 Bohren and Huffman (2007). The corresponding time series of size distribution of the derived

301 external BC and internal BC core were illustrated in Fig. S2. Thus, the $\sigma_{abs,BC,Mie, \lambda_i}$ values of

302 all six wavelengths were calculated through the Mie model, and then the AAE$_{BC}$ values of those

303 five wavelengths were obtained using Eq. (6). The performance of this empirically determined

304 calculation method has been compared with other possible BC mixing schemes in details (see

305 Table 1).

306 **2.2.4 Atmospheric radiative transfer model**

307   In this work, theSanta Barbara DISORT Atmospheric Radiative Transfer (SBDART) model

308   was employed to estimate the DRF of BrC absorption, i.e., its effects on the downward and

309   upward fluxes (F in W m^{-2}) of solar radiation at the TOA. SBDART is a software tool that can

310   be used to compute plane-parallel radiative transfer under both clear and cloudy conditions

311   within the atmosphere. More details about this model have been described by Ricchiazzi et al.

312   (1998). Both ground measurements and remote sensing data were used in the simulation. The

313   surface albedo was derived from a 500 m resolution MODIS BRDF/albedo model parameter

314   product (MCD43A3, daily). The MCD43A3 products are the total shortwave broadband black-

315   sky albedo (α_{BSA}) and white-sky albedo (α_{WSA}), while the actual surface albedo (α) was

316   computed from a linear combination of α_{WSA} and α_{BSA}, which were weighted by the diffuse ratio

317   (r_d) and direct ratio ($1-r_d$), respectively:

$$\alpha = (1 - r_d) \cdot \alpha_{BSA} + r_d \cdot \alpha_{WSA} \tag{20}$$

319   r_d was obtained from an exponential fit of Eq. (21) based on empirical observations (Roesch,

320   2004; Stokes and Schwartz, 1994):

$$r_d = 0.122 + 0.85 e^{-4.8\mu_0} \tag{21}$$

322   where μ_0 is the cosine of the zenith angle, which is calculated by the model for any specified

323   date, time, and latitude and longitude of the site. The surface-based aerosol optical properties,

324   including the aerosol light absorption coefficients of both BC and BrC, i.e., differentiated from

325   each other under the assumption of uniform AAE_{BC}, along with the nephelometer-measured

326   aerosol scattering coefficients, were used to calculate the SSA at different wavelengths

327   according to Eq. (22),

$$SSA(\lambda) = \frac{\sigma_{scat,\lambda}}{\sigma_{abs,BrC,\lambda} + \sigma_{abs,BC,\lambda} + \sigma_{scat,\lambda}} \tag{22}$$

329   which was then used in the model calculation. Finally, the AOD and asymmetry factor (ASY)

330   at 440, 675 and 870 nm were derived from the Aerosol Robotic Network (AERONET)

331   measurements at the Hong Kong Polytechnic University site (Holben et al., 1998), which is

332   approximately 115 km to the southeast of the Panyu site. The tropical atmospheric profile was

333   used in the SBDART model based on the prevailing weather conditions in the PRD. The aerosol

334   DRF (ΔF) was calculated as the difference between the downward and upward radiation fluxes:

$$\Delta F = F\downarrow - F\uparrow \tag{23}$$

3 Results and discussion

3.1 Aerosol light absorption

The AAE_{BC} is widely defined as the uniform representation of the wavelength dependence of a BC particle (Olson et al., 2015). In reality, AAE_{BC} may vary significantly with BC containing aerosols of different sizes, mixing states, and morphologies (Lack and Langridge, 2013; Scarnato et al., 2013). In fact, some studies showed that the AAE of a large-size, pure BC core may be less than 1.0 (Liu et al., 2018) and that the AAE of BC coated with a non-absorbing shell may be larger than that under uniformity (Lack and Cappa, 2010).

It has been suggested that a significant fraction of smaller size particles is non BC-containing (Cheung et al., 2016; Ma et al., 2017). BC and non-BC materials can also be externally or internally mixed. Although size resolved BC measurements were not available during this work, we have conducted size resolved Volatility Tandem Differential Mobility Analyzer (V-TDMA) measurements at 300℃ for 40, 80, 110, 150, 200 and 300 nm, respectively, during an earlier field campaign (February 2014) at the same site as in this work. At 300℃, all non-BC particle will be completely vaporized (CV) and thus the portion of non BC particles at such size, denoted as $\Phi_{N,CV}$, can be determined. The average $\Phi_{N,CV}$ values were 0.384, 0.181, 0.180, 0.158, 0.143 and 0.137, corresponding to 40, 80, 110, 150, 200 and 300 nm (see Fig. S3), respectively (Cheung et al., 2016; Tan et al., 2016a). The $\Phi_{N,CV}$ values for other sizes were interpolated linearly from these six diameters. For particle size larger than 300 nm and less than 40 nm, $\Phi_{N,CV}$ values were set to 0.137 and 0.384, respectively. Accordingly, the complete distribution of $\Phi_{N,CV}$ for the whole PNSD was obtained. The mixing states of BC particles were also estimated here, i.e., the mass portion of externally mixed BC with respect to total BC, denoted as r_{ext}. The value of r_{ext} was taken as 0.58, which was obtained using an optical closure method during a previous field experiment at this site (Tan et al., 2016a). During the following Mie theory calculation, a fixed refractive index ($\widetilde{m}_{core}$=1.80-0.54i, $\widetilde{m}_{non}$=1.55-10^{-7}i) was adopted for the whole size range. Accordingly, the calculated BC absorption at 880 nm (Abs_{880}) was 21.869 Mm^{-1}, which is reasonably close to the measured mean value of 21.199 Mm^{-1}. To further validate our calculation scheme (Base Case), we have considered several extreme cases. Case 1: BC is completely externally mixed with non-BC particles, i.e., $\Phi_{N,CV} = 0$ and $r_{ext} = 1$; Case 2: BC is present in every size bin and BC is completely internally mixed with non-BC material,

366   i.e., $\Phi_{N,CV} = 0$ and $r_{ext} = 0$; Case 3: BC is both internally and externally mixed but there is no

367   non BC-containing particles, i.e., $\Phi_{N,CV} = 0$ and $r_{ext} = 0.58$; Case 4: BC is internally mixed with

368   non-BC material and there is non-BC particles present, i.e., $\Phi_{N,CV}$ ranges from 0.384 to 0.137

369   and $r_{ext} = 0$; Case 5: the same as case 4 except assuming a fixed non-BC to BC ratio of 0.5, i.e.,

370    $\Phi_{N,CV} = 0.5$, $r_{ext} = 0$; Case 6: the same as case 5 except that some externally mixed BC is also

371   present, i.e., $\Phi_{N,CV} = 0.5$, $r_{ext} = 0.58$. The calculation results are listed in Table 1. Evidently,

372   Case 1 (complete externally mixed) will significantly underestimate the measured Abs_{880},

373   indicating that most BC particles were not likely externally mixed at the Panyu site. Complete

374   internal mixing state (Cases 2, 4, and 5), on the contrary, would substantially overestimate the

375   BC absorption regardless the form of BC core distribution function. However, when the r_{ext}

376   were considered (Case base, 3, and 6), the calculated Abs_{880} values were all very close to the

377   measured value, especially the Base Case.

378   When the AAE_{BC} was assumed to be uniform, the campaign-averaged σ_{BrC} values were

379   17.6±13.7 Mm^{-1} at 370 nm, 9.7±7.9 Mm^{-1} at 470 nm, 5.8±5.1 Mm^{-1} at 520 nm, 4.0±3.5 Mm^{-1} at

380   590 nm and 2.3±2.1 Mm^{-1} at 660 nm. At the corresponding wavelengths, BrC absorption

381   contributed 26.2±8.5%, 20.0±7.3%, 14.3±6.5%, 11.7±5.3%, and 7.8±4.1% to the total aerosol

382   absorption, respectively. When the AAE_{BC} was applied as the result of the Mie model

383   calculation, the corrected campaign-averaged $\sigma_{abs,BrC}$ values were 23.5±17.7 Mm^{-1} at 370 nm,

384   11.8±9.5 Mm^{-1} at 470 nm, 6.7±5.7 Mm^{-1} at 520 nm, 4.6±3.9 Mm^{-1} at 590 nm and 2.6±2.3 Mm^{-}

385   ^{1} at 660 nm. At the corresponding wavelengths, BrC absorption contributed 34.1±8.0%,

386   23.7±7.3%, 16.0±6.7%, 13.0±5.4%, and 8.7±4.3% to the total aerosol absorption (see Fig. 2),

387   respectively. Evidently, aerosol light absorption was predominantly due to BC; however, BrC

388   also played a significant role, especially at shorter wavelengths. Table 2 shows the inter-

389   comparison of BrC light absorption in the near UV range between this work and other studies

390   in the East Asian region. Clearly, the reported values vary substantially, and our result is toward

391   the lower end of values. Figure S4 displayed the time series of particle AAE measured by the

392   Aethalometer and AAE_{BC} was derived from Mie model calculation. The AAE_{BC} was almost

393   always lower than AAE, indicating appreciable BrC light absorption at the Panyu site.

394   **3.2 Uncertainty in BC and BrC optical differentiation**

395   Theoretically, the magnitude of BC absorptions can be affected by both parts of the complex

396 refractive indexes (RIs); thus, AAE_{BC} may also vary with the RIs of both the BC core and

397 coating shell. In fact, RI was also one of the least known properties of BC and other coating

398 materials with negligible absorbing capabilities. The refractive index of the BC core ($\widetilde{m}_{core}$)

399 displays a wide range of variations (Liu et al., 2018). Typically, the real and imaginary parts of

400 the RI can vary from 1.5 to 2.0 and 0.5 to 1.1, respectively. In addition, the shell was assumed

401 to consist of non-absorbing material in the core-shell model, i.e., its imaginary RI was set to be

402 close to zero (10^{-7}). The real part of the non-absorbing material RI ($\widetilde{m}_{non}$) may vary from 1.35

403 to 1.6 due to the presence of OA (Redmond and Thompson, 2011; Zhang et al., 2018) and

404 inorganic salts (Erlick et al., 2011). Hence, it is necessary to investigate the uncertainties

405 associated with the variations in AAE_{BC} by varying the RIs of both the BC core and the non-

406 absorbing materials.

407 Figure 3 shows the impacts of RI on the evaluations of AAE_{BC} based on core-shell and external

408 configuration, where the RI of the BC core was set to be constant, i.e., $\widetilde{m}_{core}=1.80-0.54i$, and

409 the real part of $\widetilde{m}_{non}$ varied from 1.35 to 1.6 at an interval of 0.05, with the imaginary part of

410 $\widetilde{m}_{non}$ set at 10^{-7}. As shown in Fig. 3a, the calculated AAE_{BC} for the core-shell model was higher

411 than 1.0 at longer wavelengths (520 to 880 nm) and lower than 1.0 at shorter wavelengths (370

412 to 520 nm) (the red line in Fig. 3 denotes $AAE_{BC}=1$). The averaged $AAE_{BC,370-520nm}$ ranged from

413 0.84 to 0.87, and the $AAE_{BC,520-880nm}$ ranged from 1.07 to 1.15, indicating that the $AAE_{BC,520-880nm}$

414 $_{880nm}$ appeared to be more sensitive to the shell's real part than $AAE_{BC,370-520nm}$. Even if the shell

415 material was assumed to be non-absorbing, the variation in the real RI of the shell, which was

416 referred to as the real part of $\widetilde{m}_{non}$, still led to changes in the shell's refractivity and

417 correspondingly altered its lensing effect, causing a change in AAE_{BC}. Meanwhile, $AAE_{BC,370-520nm}$

418 $_{520nm}$ and $AAE_{BC,520-880nm}$ generally increased with an increasing real part of the shell. In Fig. 3b,

419 under the externally mixed conditions, $AAE_{BC,370-520nm}$ and $AAE_{BC,520-880nm}$ were both less than

420 1.0. The average $AAE_{BC,370-520nm}$ was 0.33, and the average $AAE_{BC,520-880nm}$ was 0.63. These

421 values were far less than the values under core-shell mixture conditions. In the external mixture

422 model, the BC core and nonlight-absorbing materials were assumed to exist dependently, and

423 then the optical properties of these two components were considered separately. Therefore,

424 altering the real part of the externally mixed non-absorbing material would not affect the light

425 absorption property of the BC core or AAE_{BC}.

426 The impacts of the BC core on AAE_{BC} are shown in Fig. 4, where the refractive index of

427 nonlight-absorbing materials was assumed to be $\tilde{m}_{non}$=1.55-10^{-7}i and $\tilde{m}_{non}$ was wavelength-

428 independent. Figure 4 was obtained with a core-shell mixture model (Fig. 4a and 4b) and an

429 external mixture model (Fig. 4c and 4d) by varying the real part of $\tilde{m}_{core}$ from 1.5 to 2.0 with

430 a step of 0.05 and varying the imaginary part of the $\tilde{m}_{core}$ from 0.4 to 1.0 with a step of 0.05,

431 respectively. As shown in Figs. 4a and 4b, for the core-shell mixture, the averaged $AAE_{BC,370-}$

432 $_{520nm}$ ranged from 0.55 to 0.99, and the averaged $AAE_{BC,520-880nm}$ ranged from 0.84 to 1.27. The

433 AAE_{BC} at a certain wavelength generally increased when increasing the real part of $\tilde{m}_{core}$ but

434 decreased when increasing the imaginary part of $\tilde{m}_{core}$. The AAE_{BC} appeared to be more

435 sensitive to the imaginary part of $\tilde{m}_{core}$ than the real part of $\tilde{m}_{core}$ because the imaginary part

436 of $\tilde{m}_{core}$ was directly related to the light-absorbing properties of particles. In Figs. 4c and 4d,

437 for the external mixture, the averaged $AAE_{BC,370-520nm}$ ranged from 0.04 to 0.45 and the averaged

438 $AAE_{BC,520-880nm}$ ranged from 0.28 to 0.79, while the averaged $AAE_{BC,370-520nm}$ and $AAE_{BC,520-}$

439 $_{880nm}$ were both less than 1.0. Similar to the core-shell mixture, the $AAE_{BC,520-880nm}$ increased

440 when increasing the real part of $\tilde{m}_{core}$ but decreased when increasing the imaginary part of

441 $\tilde{m}_{core}$. However, the variation patterns of $AAE_{BC,370-520nm}$ were different from those of $AAE_{BC,520-}$

442 $_{880nm}$. The $AAE_{BC,370-520nm}$ values were not changed by altering the real part of $\tilde{m}_{core}$ within the

443 low imaginary part of $\tilde{m}_{core}$, whereas the $AAE_{BC,370-520nm}$ values still increased when increasing

444 the real part of $\tilde{m}_{core}$ within the high imaginary part of $\tilde{m}_{core}$. A possible explanation was that

445 the externally mixed BC core had weak light absorption within the low imaginary part of $\tilde{m}_{core}$,

446 causing the $AAE_{BC,370-520nm}$ values to be insensitive to the real part of $\tilde{m}_{core}$. The $AAE_{BC,520-}$

447 $_{880nm}$ values were higher than the $AAE_{BC,370-520nm}$ values regardless of whether in they were for

448 the core-shell mixture or external mixture. In addition, the AAE_{BC} values conducted by the

449 core-shell mixture were higher than those conducted by the external mixture.

450 Figure 4 demonstrated that the variation in the imaginary RI of the BC core had the most

451 significant impact on the estimated AAE_{BC}, indicating that the chemical component of BC

452 emitted from different sources led to a large uncertainty in AAE_{BC} estimation. At the same time,

453 the influence arising from varying the real RI of the BC core was relatively moderate.

454 Nevertheless, Fig. 3 showed that change in the real RI of the non-absorbing materials caused

455 the least/no impact compared to that caused by the variations in the complex RI of the BC core.

456 It should be pointed out that most BC-containing particles are often observed as fractal rather

457 than spherical in shape (Katrinak et al., 1993). Because the Mie model assumes that all particles

458 are spherical, it may lead to potential uncertainty for the estimation of AAE_{BC} and BrC

459 absorption contributions. Moreover, the externally mixed soot aggregates were "chain-like" or

460 "puff-like" in the PRD dry season (Feng et al., 2010), in which the fractal dimension (D_f) was

461 between 1.5 and 2.0. Coating soot aggregates were likely sphere (D_f approaches 3) from the

462 high-resolution transmission electron microscopy (TEM) measurements taken in Hongkong

463 (Zhou et al., 2014). A soot aggregate sensitivity study with the superposition T-matrix method

464 indicated that using the assumption of volume-equivalent spheres for the soot aggregates may

465 result in an overestimation of approximately up to 15% and an underestimation of

466 approximately up to 50% in the predicted 870 nm light absorption when the D_f is between 1.5

467 and 3.0 (Liu et al., 2008). However, it should be recognized that the complex shapes or positions

468 of the BC core inside the particle make it impractical to be numerically simulated in the exact

469 details. By far the Mie model with a core-shell configuration would be the most practical and

470 effective simulation scheme for BC particle optical property simulation.

471 Furthermore, we have performed Monte Carlo simulations to evaluate the uncertainties of the

472 Mie calculation performed during this work. In the simulation, a sequence of random numbers

473 or errors were applied to the input parameters, and then the corresponding uncertainties of

474 particle light absorption and AAE_{BC} were computed using the Mie model. Five hundred of

475 reiteration were conducted during the simulation such that the random errors will be normally

476 distributed. The standard deviations (σ) of all input parameters are listed in Table S1. In order

477 to cover the effect of extreme value, we used a range of $\pm 3\sigma$, or a confidence level of 99%, in

478 the Monte Carlo simulation. Table S2 listed the Monte Carlo simulation results, i.e., the average

479 relative standard deviations (σ_{Mie}) of the calculated BC light absorption at 880 nm (Abs_{880}),

480 $AAE_{BC,370-520}$, and $AAE_{BC,520-880}$. The uncertainties of the calculated Abs_{880}, $AAE_{BC,370-520}$, and

481 $AAE_{BC,520-880}$ at two times of σ_{Mie}, i.e., at a confidence level of 95%, were approximately $\pm 31\%$,

482 $\pm 16\%$, and $\pm 13\%$, respectively. Figure S5a showed the time series of the uncertainties of Abs_{880},

483 $AAE_{BC,370-520}$ and $AAE_{BC,520-880}$ from Monte Carlo simulation for the campaign period. These

484 uncertainties will certainly be propagated into the calculated BrC absorption contributions, too.

485 Hence, we also estimated the corresponding uncertainties in the BrC absorption contribution

486 results, as shown in Fig. S5b. Accordingly, the averaged lower limits of BrC absorption

487 contributions were 26.8%±9.1% at 370 nm, 17.5%±8.1% at 470 nm, 10.1%±7.3% at 520 nm,

488 8.5%±5.8% at 590 nm and 5.3%±4.5% at 660 nm, respectively, and the averaged upper limits

489 of BrC absorption contribution ratios were 40.7%±7.2% at 370 nm, 29.5%±6.7% at 470 nm,

490 21.1%±6.2% at 520 nm, 17.3%±5.2% at 590 nm and 12.0%±4.1% at 660 nm, respectively.

3.3 Characteristics of BrC light absorption, water-soluble ions and OC concentrations

492 Globally, BrC has been observed to be highly correlated with biomass and biofuel burning

493 emissions (Laskin et al., 2015). Since large quantities of sylvite are present in biomass burning

494 particles, the K^+ abundance has often been used as a biomass burning tracer (Levine, 1991).

495 Figure 5 presents the time series of the OC mass concentration, K^+ concentration, and BrC

496 absorption from 29 November 2014 to 2 January 2015 at the Panyu site. The range of the OC

497 concentration obtained from the OC/EC online analyzer was from 1.5 to 65.2 $\mu g\ cm^{-3,}$ and the

498 campaign average was 12.5±7.3 $\mu g\ cm^{-3}$. The BrC absorption hourly mean data were between

499 0.2 and 123.2 $Mm^{-1,}$ and the campaign average was 23.5±17.7 Mm^{-1}. On the other hand, the

500 average K^+ concentration was 1.0 ± 0.7 $\mu g\ cm^{-3}$ (ranging from 0 to 5.4 $\mu g\ cm^{-3}$). Clearly, similar

501 trends among OC, K^+, and BrC absorption can be seen during this field campaign (Fig. 5).

502 To investigate the origins of these observed OC, K^+, and BrC, wind rose plots (as shown in Fig.

503 6) were generated for OC, K^+, and BrC absorption, respectively. All three panels of Fig. 6

504 consistently show that the three substances were associated with the same wind pattern. For the

505 entire campaign period, the highest values of OC, K^+, and $\sigma_{abs,BrC,370nm}$ were mostly associated

506 with southwesterly winds with a relatively low wind speed (~2 m s^{-1}). The relatively higher OC

507 and K^+ concentrations were highly related to the seasonal straw burning in the countryside of

508 the PRD located to the west of the Panyu station. In contrast, OC and K^+ concentrations during

509 periods with easterly winds were substantially lower than those during periods with westerly

510 winds. The wind rose plot of $\sigma_{abs,BrC,370nm}$ is shown in Fig. 6c. Similar to OC and K^+, $\sigma_{abs,BrC,370nm}$

511 showed higher values under weak (<2 m s^{-1}) westerly winds and lower values from the north

512 and south, indicating that BrC absorption was likely attributed to local sources and was

513 accumulated under calm wind conditions. Figure S6 showed the 3-day backward trajectory and

514 the fire counts for 5 to 7 (Fig. S6a), 12 to 14 (Fig. S6b) and 24 to 26 (Fig. S6c) in November

515 2014, representing low loading, moderate loading and high loading period. Clearly, the high

516 loading period concurred with stagnant air movement and higher fire counts, indicating the

517 contribution from open fire burning sources. However, there was a detectable difference among

518 the three rose plots of Fig. 6 in the maximum concentration direction. A possible explanation

519 was that although biomass burning emissions were believed to be the dominant and primary

520 source of OC, K^+, and BrC, their emission ratios were highly variable and may change with the

521 type of biofuel and burning condition and may even vary during different stages of burning

522 (Burling et al., 2012). Although biomass burning emissions contain substantial light-absorbing

523 BrC, further atmospheric aging processes may significantly reduce its light-absorbing

524 capability (Satish et al., 2017). Moreover, secondary formation may also lead to BrC formation

525 inside these primary aerosols, such as humic-like substances formed through aqueous-phase

526 reactions, which have been suggested to be an important component of BrC (Andreae and

527 Gelencser, 2006).

528 To further explore the possible sources of BrC optical absorption, the diurnal variations in OC,

529 K^+, $\sigma_{abs,BrC,370nm}$, and $\sigma_{abs,BrC,370nm}$ /OC values are plotted in Fig. 7. The diurnal variation in OC

530 at the Panyu site appeared to be dominated by the development of the planetary boundary layer

531 (PBL) height, i.e., primary emissions accumulated at night and were swiftly diluted by vertical

532 mixing in the morning. The slight increase in OC in the afternoon indicated that photochemistry

533 may have still weakly contributed to SOA formation. Fig. 7b shows the diurnal variation in K^+.

534 Unlike OC, K^+ shows a small peak at approximately 6 AM, which was consistent with breakfast

535 time and was very likely due to cooking activities using biofuel. No lunch and dinner time K^+

536 peaks were observed. The most likely explanation is that the boundary layer height is much

537 higher during lunch and dinner time than in the early morning, providing a much better

538 atmospheric diffusion condition for air pollutants. It is still a common practice to collect straw

539 as biofuel in local rural areas, which can be visually spotted but is not heavily utilized in the

540 region. However, the diurnal profile of $\sigma_{abs,BrC,370nm}$ (see Fig. 7c) shows the combined features

541 of OC and K^+ since both primary and secondary processes affect its intensity. The nighttime

542 increasing trend was most likely attributed to straw burning activities in early winter in nearby

543 rural areas that continued to accumulate within the shallow PBL (Jiang et al., 2013).

544 $\sigma_{abs,BrC,370nm}$/OC, i.e., the mass absorption coefficient of BrC (MAC$_{BrC}$) (Fig. 7d), showed a

545 relatively flat pattern, with a pronounced dip in the afternoon and higher values at nighttime,

546   which was likely due to enhanced primary emissions and stable stratification at nighttime.

547   Declining trends during the late morning and afternoon hours indicated that the aging process

548   and photochemical production may reduce the light-absorbing capacity of BrC (Qin et al.,

549   2018).

550   Furthermore, Fig. 8 shows the linear regression analysis results used to evaluate the correlations

551   of $\sigma_{abs,BrC,370nm}$ with the OC, K^+, Ca^{2+}, Mg^{2+}, Cl^-, SO_4^{2-}, NO_3^-, and NH_4^+ concentrations. The best

552   correlations can be found between $\sigma_{abs,BrC,370nm}$ and K^+ (R^2=0.6148), followed by those between

553    $\sigma_{abs,BrC,370nm}$ and OC (R^2=0.4514), NO_3^- (R^2=0.4224) and NH_4^+ (R^2=0.4656). Source

554   apportionment analysis of OA and BrC absorption in Beijing and Guangzhou illustrated that

555   biomass burning organic aerosols (BBOAs) correlated well with BrC light absorption (Qin et

556   al., 2018; Xie et al., 2018). Thus, the significant correlation between BrC absorption and K^+

557   reaffirmed that biomass burning was the crucial emission source of BrC observed in this work.

558   Although the geographic location of the observation site was situated in a coastal area and K^+

559   could also be found in sea salt (Pio et al., 2008), it should be noted that the prevailing wind

560   direction during winter was from the north (see Fig. S6), which drives maritime air parcels

561   away from the site. Hence, the effect of sea salt and crustal materials to K^+ was slight, which

562   was demonstrated in the supplementary information as shown in Fig. S7. Other earlier studies

563   also suggested that the sea salt contribution to the K^+ concentrations of $PM_{2.5}$ was trivial in the

564   PRD region during the winter (Lai et al., 2007). Another possible K^+ source was coal

565   combustion. The coal consumption in the PRD region was dominated by coal-fired power

566   plants. The emission from power plants was usually very steady and was less likely to affect

567   the diurnal correlation between K^+ and BrC absorption. As shown in Fig. S8, the ratios of

568    $K^+/PM_{2.5}$ varies approximately from 0.015 and 0.020 and the diurnal profile of $K^+/PM_{2.5}$ shows

569   very little variation. Yu et al. (2018) have suggested that K^+ usually accounted for 2.34-5.49%

570   of $PM_{2.5}$ in the laboratory biomass burning study. However, K^+ was normally lower than 1% of

571   coal combustion $PM_{2.5}$. Therefore, the ratio range of K^+ to $PM_{2.5}$ observed in this work likely

572   indicated aged biomass burning particles. Both nitrogen oxides (NO_x) and ammonia (NH_3) can

573   be found in biomass burning plumes (Andreae and Merlet, 2001). For NO_3^- and NH_4^+, nitrate

574   can be converted from NO_x through atmospheric reactions, and ammonium may originate from

575   NH_3. However, similar to the diurnal variation in $\sigma_{abs,BrC,370nm}$, diurnal variations in NH_4^+ and

576 NO_3^- also increased in the afternoon and appeared at nighttime in Fig. S8. However, $NO_3^-/PM_{2.5}$

577 and $NH_4^+/PM_{2.5}$ reached their peaks at noon, indicating that ammonium nitrate formed from the

578 secondary reaction at this time. Along with the reduced boundary layer height and ambient

579 temperature, NO_3^- was accumulated until the photochemical reaction stopped at night. The

580 diurnal variation in NH_4^+ was similar to that in NO_3^- due to the acid/base neutralization reaction.

581 The overlapping of the $\sigma_{abs,BrC,370nm}$, NH_4^+ and NO_3^- diurnal variations would lead to a significant

582 correlation between BrC absorption and NO_3^- or NH_4^+. High concentrations of Ca^{2+} and Mg^{2+}

583 are often found in dust-related aerosols (Lee et al., 1999). $\sigma_{abs,BrC,370nm}$ showed poor correlations

584 with both Ca^{2+} and Mg^{2+}, indicating that dust-related aerosol components contribute

585 insignificantly to the total aerosol mass loading and, thus, dust may not affect the AAE

586 differentiation method used in this work. Although sulfur dioxide (SO_2) may also be emitted by

587 biomass burning, SO_4^{2-} is often believed to be secondary in nature, and the presence of other

588 intense SO_2 sources (e.g., automobile and industrial emissions) further reduces the correlation

589 between BrC and SO_4^{2-}. Sources of Cl^- include both combustion and sea salt spray (Waldman

590 et al., 1991). Although the prevailing wintertime wind direction was from the north, sea salt

591 can still be carried to the site by a weak sea breeze, and thus, Cl^- may not show considerable

592 correlation with BrC.

593 **3.4 BrC radiative forcing efficiency**

594 The radiative effects of aerosol scattering, BrC absorption, and BC absorption were investigated

595 by the SBDART model. For each investigated variable under cloud-free conditions, we run the

596 model twice to calculate the DRF at the TOA with and without the investigated variable.

597 Accordingly, the difference of ΔF between the two simulations was considered as the radiative

598 effect of the investigated variable. The results showed that the average radiative forcings at the

599 TOA by scattering, BrC absorption, and BC absorption were -21.4±5.5 W m^{-2}, 2.3±1.8 W m^{-2},

600 and 10.9±5.1 W m^{-2}, respectively. Furthermore, BrC absorption was attributed to 15.8±4.4%

601 of the warming effect caused by aerosol light absorption, demonstrating the nonnegligible role

602 of BrC in radiative forcing evaluation.

603 We also calculated the BrC radiative forcing efficiency (RFE) under various SSA (ranging from

604 0.70 to 0.99) at three wavelengths, i.e., 440 nm, 675 nm, and 870 nm. The RFE was denoted as

605 the radiative forcing normalized by the AOD. The average AOD and ASY at the three

606   wavelengths were 0.365 and 0.691 at 440 nm, 0.212 and 0.632 at 675 nm, and 0.154 and 0.619

607   at 870 nm, respectively. A solar zenith angle of 55° and an average shortwave broadband surface

608   albedo (0.119) were used in the calculation. The results were plotted as a set of RFE lookup

609   charts as a function of the surface BrC absorption contribution (see Fig. 9).

610   In general, for any wavelength, the RFE increased with increasing BrC absorption contribution

611   for a certain SSA, indicating that BrC was a more efficient radiative forcing agent due to the

612   preferential absorbance of BrC in a shorter wavelength range. However, for a certain BrC

613   absorption contribution, the RFE increased with decreasing SSA, i.e., a higher portion of light-

614   absorbing aerosol components can lead to more efficient radiative forcing. The trend among

615   panels (a), (b), and (c) in Fig. 9 demonstrated that the effect of BrC absorption contribution on

616   RFE was wavelength-dependent, i.e., BrC was a weaker radiative forcing agent at longer

617   wavelengths, which is also consistent with the wavelength-dependent light-absorbing property

618   of BrC. The red stars in Fig. 9 denote the average SSA and BrC absorption contribution

619   conditions during this campaign, i.e., 0.029 W m^{-2} per unit AOD at 440 nm (Fig. 9a), 0.007 W

620   m^{-2} per unit AOD at 675 nm (Fig. 9b), and 0.0002 W m^{-2} per unit AOD at 870 nm (Fig. 9c).

621   These results suggested that the average value of RFE decreased distinctly from 440 nm to 870

622   nm not only because of the lower BrC absorption contribution but also because of the

623   wavelength-dependence of the BrC RFE. It should also be noted that the simulations were based

624   on SSA measured under dry conditions. Under the typical ambient conditions of the PRD, the

625   SSA might be markedly enhanced by aerosol water uptake (Jung et al., 2009), and then, the BrC

626   radiative forcing efficiency might be less. Moreover, Fig. 9 also serves as a lookup table to

627   conveniently assess the BrC radiative forcing efficiency at different wavelengths with different

628   BrC absorption contributions for a certain SSA.

629   **4 Conclusion**

630   In this work, light absorption due to BrC in the PRD region of China was quantitatively deduced

631   during the winter season of 2014. The AAE of ambient particles and BC core were derived

632   from the measurements. For ambient particles, $AAE_{370-520nm}$ and $AAE_{520-880nm}$ ranged from 0.81

633   to 2.31 and 0.91 to 2.13, respectively. In the case of BC, $AAE_{BC,370-520nm}$ and $AAE_{BC,520-880nm}$

634   ranged from 0.59 to 0.98 and 0.82 to 1.15, respectively. Using the absorption coefficients of

635   BC calculated according to the Mie theory and the observed total aerosol absorption coefficients,

636   we estimated the AAE_{BC} and hence the BrC absorption contribution for the optically equivalent

637   mixture configuration. The average BrC light absorption contribution ranged from 8.7±4.3% at

638   660 nm up to 34.1±8.0% at 370 nm when AAE_{BC} was set as uniform. The sensitivity of AAE_{BC}

639   estimation associated with different RI and mixing state assumptions was further investigated.

640   The results showed that variations in the real RI of the non-absorbing material (1.35 to 1.6) may

641   increase $AAE_{BC,370-520nm}$ from 0.84 to 0.87 and $AAE_{BC,520-880nm}$ from 1.07 to 1.15 for core-shell

642   mixtures, with an $AAE_{BC,370-520nm}$ of 0.33 and $AAE_{BC,520-880nm}$ of 0.63 for external mixtures.

643   Variations in the core's real RI (1.5 to 2.0) and imaginary RI (1.0 to 0.4) may increase $AAE_{BC,370-}$

644    $_{520nm}$ from 0.55 to 0.99 and $AAE_{BC,520-880nm}$ from 0.84 to 1.27 for the core-shell mixture and

645   increase $AAE_{BC,370-520nm}$ from 0.04 to 0.45 and $AAE_{BC,520-880nm}$ from 0.28 to 0.79 for the external

646   mixture. These results indicate that the optical properties of the BC core and non-absorbing

647   material can significantly affect the accuracy of AAE_{BC} and corresponding BrC absorption

648   contribution estimations. Compared to the values of BrC light absorption coefficient and BrC

649   light absorption contribution from other similar studies conducted in the East Asia region, the

650   BrC measured in this work showed relatively lower values of light absorption coefficient but

651   was found responsible for relatively higher portion of light absorption. It should be noted that

652   the calculated BrC light absorption may vary exponentially with the value of AAE_{BC}. According

653   to Monte Carlo simulations under 95% confidence level, we found that BrC light absorption

654   contribution ratios in this work can range roughly from 18% to 48% at 370 nm, 10% to 37% at

655   470 nm, 3% to 27% at 520 nm, 3% to 22% at 590 nm, and 1% to 16% at 660 nm, respectively.

656   Therefore, proper values of AAE_{BC} have to be carefully obtained for a particular study area,

657   especially needed to be constrained by the BC mass concentration, size-distribution, and mixing

658   state measurements.

659   Additionally, the measurements of major water-soluble inorganic ions (including K^+, NO_3^-, and

660   NH_4^+) and particulate OC showed consistent features with those of $\sigma_{abs,BrC,370nm}$, implying that

661   BrC was associated with biomass-burning emissions from nearby rural areas. Moreover, the

662   diurnal trend in $\sigma_{abs,BrC,370nm}$/OC indicated that primary biomass burning emissions can produce

663   intense light-absorbing BrC, while the photochemical aging process may weaken the light-

664   absorbing capability of BrC.

665   Using a radiative transfer model (i.e., SBDART), we estimated the BrC effects on aerosol

radiative forcing. The average shortwave aerosol direct radiative forcings due to scattering, BrC absorption, and BC absorption at the TOA were evaluated to be -21.4±5.5 W m^{-2}, 2.3±1.8 W m^{-2}, and 10.9±5.1 W m^{-2}, respectively. BrC absorption accounted for 15.8±4.4% of the total shortwave solar absorption warming effect at the TOA, indicating that BrC might be an important climate forcing agent, which is largely neglected in current climate models. To facilitate the estimation of the climate effects of BrC, a set of look-up charts was constructed for the investigated area based on the default tropical atmosphere profile, average surface albedo, average asymmetry factor, and surface-measured aerosol properties (i.e., BrC absorption contribution, *SSA*, and AOD). Therefore, the role of the BrC radiative forcing efficiency at three wavelengths can be conveniently assessed for certain *SSA* and BrC absorption contributions.

Author contributions

HT, JZ, YM, and CC designed the experiments, and ZL, LL, YQ, NW, FL, YL, and MC carried out the field measurements and data analysis. ZL and YQ performed Mie theory simulation. ZL, JZ, and HT prepared the manuscript with comments from all coauthors.

Acknowledgements

This work is supported by the National Key Project of MOST (2016YFC0201901, 2016YFC0203305, and 2016YFC0202401), the National Natural Science Foundation of China (41575122 and 41730106), and the National Research Program for Key Issues in Air Pollution Control (No. DQGG0103). We are also deeply thankful for Dr. Wu and the staff at the Hong Kong Polytechnic University site of AERONET.

References:

Andreae, M. O., and Merlet, P.: Emission of trace gases and aerosols from biomass burning, Global Biogeochem. Cycles, 15, 955-966, 2001.

Andreae, M. O., and Gelencser, A.: Black carbon or brown carbon? The nature of light-absorbing carbonaceous aerosols, Atmospheric Chemistry & Physics, 6, 3131-3148, 2006.

Ångström, A.: On the Atmospheric Transmission of Sun Radiation and on Dust in the Air, Geografiska Annaler, 11, 156-166, 1929.

697 Arnott, W. P., Hamasha, K., Moosmüller, H., Sheridan, P. J., and Ogren, J. A.: Towards Aerosol
698 Light-Absorption Measurements with a 7-Wavelength Aethalometer: Evaluation with a
699 Photoacoustic Instrument and 3-Wavelength Nephelometer, Aerosol Science and Technology,
700 39, 17-29, 10.1080/027868290901972, 2005.

701 Arola, A., Schuster, G. L., Pitkänen, M. R. A., Dubovik, O., Kokkola, H., Lindfors, A. V.,
702 Mielonen, T., Raatikainen, T., Romakkaniemi, S., Tripathi, S. N., and Lihavainen, H.: Direct
703 radiative effect by brown carbon over the Indo-Gangetic Plain, Atmospheric Chemistry and
704 Physics, 15, 12731-12740, 10.5194/acp-15-12731-2015, 2015.

705 Bauer, J. J., Yu, X.-Y., Cary, R., Laulainen, N., and Berkowitz, C.: Characterization of the
706 Sunset Semi-Continuous Carbon Aerosol Analyzer, Journal of the Air & Waste Management
707 Association, 59, 826-833, 10.3155/1047-3289.59.7.826, 2012.

708 Bodhaine, B. A.: Aerosol absorption measurements at Barrow, Mauna Loa and the south pole,
709 Journal of Geophysical Research Atmospheres, 100, 8967–8975, 1995.

710 Bohren, C. F., and Huffman, D. R.: Wiley: Absorption and Scattering of Light by Small
711 Particles - Craig F. Bohren, Donald R. Huffman, Optics & Laser Technology, 31, 328-328, 1983.

712 Bohren, C. F., and Huffman, D. R.: Absorption and Scattering of Light by Small Particles,
713 WILEY‐VCH Verlag GmbH & Co. KGaA 328-328 pp., 2007.

714 Bond, T. C., Streets, D. G., Yarber, K. F., Nelson, S. M., Woo, J. H., and Klimont, Z.: A
715 technology-based global inventory of black and organic carbon emissions from combustion, J.
716 Geophys. Res.-Atmos., 109, 43, 10.1029/2003jd003697, 2004.

717 Bond, T. C., Zarzycki, C., Flanner, M. G., and Koch, D. M.: Quantifying immediate radiative
718 forcing by black carbon and organic matter with the Specific Forcing Pulse, Atmospheric
719 Chemistry and Physics, 11, 1505-1525, 10.5194/acp-11-1505-2011, 2011.

720 Bricaud, A., and Morel, A.: Light attenuation and scattering by phytoplanktonic cells: a
721 theoretical modeling, Applied Optics, 25, 571, 10.1364/ao.25.000571, 1986.

722 Burling, I. R., Yokelson, R. J., Akagi, S. K., Urbanski, S. P., Wold, C. E., Griffith, D. W. T.,
723 Johnson, T. J., Reardon, J., and Weise, D. R.: Airborne and ground-based measurements of the
724 trace gases and particles emitted by prescribed fires in the United States (vol 11, pg 12197,
725 2011), Atmospheric Chemistry and Physics, 12, 103-103, 10.5194/acp-12-103-2012, 2012.

726 Chan, C. K., and Yao, X.: Air pollution in mega cities in China, Atmospheric Environment, 42,
727 1-42, http://dx.doi.org/10.1016/j.atmosenv.2007.09.003, 2008.

728 Cheng, Y., He, K. B., Zheng, M., Duan, F. K., Du, Z. Y., Ma, Y. L., Tan, J. H., Yang, F. M., Liu,
729 J. M., Zhang, X. L., Weber, R. J., Bergin, M. H., and Russell, A. G.: Mass absorption efficiency
730 of elemental carbon and water-soluble organic carbon in Beijing, China, Atmospheric
731 Chemistry and Physics, 11, 11497-11510, 10.5194/acp-11-11497-2011, 2011.

732 Cheng, Y. F., Eichler, H., Wiedensohler, A., Heintzenberg, J., Zhang, Y. H., Hu, M., Herrmann,
733 H., Zeng, L. M., Liu, S., Gnauk, T., Brüggemann, E., and He, L. Y.: Mixing state of elemental
734 carbon and non-light-absorbing aerosol components derived from in situ particle optical
735 properties at Xinken in Pearl River Delta of China, Journal of Geophysical Research:
736 Atmospheres, 111, doi:10.1029/2005JD006929, 2006.

737 Cheung, H. H. Y., Tan, H., Xu, H., Li, F., Wu, C., Yu, J. Z., and Chan, C. K.: Measurements of
738 non-volatile aerosols with a VTDMA and their correlations with carbonaceous aerosols in
739 Guangzhou, China, Atmospheric Chemistry and Physics, 16, 8431-8446, 10.5194/acp-16-
740 8431-2016, 2016.

741 Coen, M. C., Weingartner, E., Apituley, A., Ceburnis, D., Fierzschmidhauser, R., Flentje, H.,
742 Henzing, J. S., Jennings, S. G., Moerman, M., and Petzold, A.: Minimizing light absorption
743 measurement artifacts of the Aethalometer: evaluation of five correction algorithms,
744 Atmospheric Measurement Techniques, 3, 457-474, 2010.

745 Desyaterik, Y., Sun, Y., Shen, X., Lee, T., Wang, X., Wang, T., and Collett, J. L.: Speciation of
746 "brown" carbon in cloud water impacted by agricultural biomass burning in eastern China,
747 Journal of Geophysical Research: Atmospheres, 118, 7389-7399, 10.1002/jgrd.50561, 2013.

748 Drinovec, L., Močnik, G., Zotter, P., Prévôt, A. S. H., Ruckstuhl, C., Coz, E., Rupakheti, M.,
749 Sciare, J., Müller, T., Wiedensohler, A., and Hansen, A. D. A.: The "dual-spot" Aethalometer:
750 an improved measurement of aerosol black carbon with real-time loading compensation,
751 Atmospheric Measurement Techniques, 8, 1965-1979, 10.5194/amt-8-1965-2015, 2015.

752 Erlick, C., Abbatt, J. P. D., and Rudich, Y.: How Different Calculations of the Refractive Index
753 Affect Estimates of the Radiative Forcing Efficiency of Ammonium Sulfate Aerosols, Journal
754 of the Atmospheric Sciences, 68, 1845-1852, 10.1175/2011jas3721.1, 2011.

755 Feng, X., Dang, Z., Huang, W., Shao, L., and Li, W.: Microscopic morphology and size
756 distribution of particles in PM2.5 of Guangzhou City, Journal of Atmospheric Chemistry, 64,
757 37-51, 10.1007/s10874-010-9169-7, 2010.

758 Feng, Y., Ramanathan, V., and Kotamarthi, V. R.: Brown carbon: a significant atmospheric
759 absorber of solar radiation?, Atmospheric Chemistry and Physics, 13, 8607-8621, 10.5194/acp-
760 13-8607-2013, 2013.

761 Hoffer, A., Gelencsér, A., Guyon, P., and Kiss, G.: Optical properties of humic-like substances
762 (HULIS) in biomass-burning aerosols, Atmospheric Chemistry & Physics, 5, 3563-3570, 2005.

763 Holben, B. N., Eck, T. F., Slutsker, I., Tanré, D., Buis, J. P., Setzer, A., Vermote, E., Reagan, J.
764 A., Kaufman, Y. J., and Nakajima, T.: AERONET—A Federated Instrument Network and Data
765 Archive for Aerosol Characterization, Remote Sensing of Environment, 66, 1-16, 1998.

766 Huang, R.-J., Zhang, Y., Bozzetti, C., Ho, K.-F., Cao, J.-J., Han, Y., Daellenbach, K. R., Slowik,
767 J. G., Platt, S. M., Canonaco, F., Zotter, P., Wolf, R., Pieber, S. M., Bruns, E. A., Crippa, M.,
768 Ciarelli, G., Piazzalunga, A., Schwikowski, M., Abbaszade, G., Schnelle-Kreis, J.,

769 Zimmermann, R., An, Z., Szidat, S., Baltensperger, U., Haddad, I. E., and Prevot, A. S. H.:
770 High secondary aerosol contribution to particulate pollution during haze events in China,
771 Nature, 514, 218-222, 10.1038/nature13774
772 http://www.nature.com/nature/journal/v514/n7521/abs/nature13774.html#supplementary-
773 information, 2014.

774 Jiang, D., Wang, C., Wu, D., Deng, X., Huang, X., Tan, H., Li, F., and Deng, T.: Diurnal
775 variation of atmospheric boundary layer over Wushan station, Guangzhou using wind profiler
776 radar   (in Chinese), Journal of Tropical Meteorology, 29, 129-135, 2013.

777 Jung, J., Lee, H., Kim, Y. J., Liu, X., Zhang, Y., Gu, J., and Fan, S.: Aerosol chemistry and the
778 effect of aerosol water content on visibility impairment and radiative forcing in Guangzhou
779 during the 2006 Pearl River Delta campaign, Journal of Environmental Management, 90, 3231-
780 3244, http://dx.doi.org/10.1016/j.jenvman.2009.04.021, 2009.

781 Katrinak, K. A., Rez, P., Perkes, P. R., and Buseck, P. R.: Fractal geometry of carbonaceous
782 aggregates from an urban aerosol, Environmental Science & Technology, 27, págs. 225-238,
783 1993.

784 Khalizov, A. F., Xue, H., Wang, L., Zheng, J., and Zhang, R.: Enhanced light absorption and
785 scattering by carbon soot aerosol internally mixed with sulfuric acid, The journal of physical
786 chemistry. A, 113, 1066-1074, 10.1021/jp807531n, 2009.

787 Kirchstetter, T. W., Novakov, T., and Hobbs, P. V.: Evidence that the spectral dependence of
788 light absorption by aerosols is affected by organic carbon, Journal of Geophysical Research:
789 Atmospheres, 109, n/a-n/a, 10.1029/2004jd004999, 2004.

790 Kulkarni, P., Baron, P. A., and Willeke, K.: Aerosol measurement : principles, techniques, and
791 applications, Van Nostrand Reinhold, 807-808 pp., 1996.

792 Lack, D. A., and Cappa, C. D.: Impact of brown and clear carbon on light absorption
793 enhancement, single scatter albedo and absorption wavelength dependence of black carbon,
794 Atmospheric Chemistry and Physics, 10, 4207-4220, 10.5194/acp-10-4207-2010, 2010.

795 Lack, D. A., and Langridge, J. M.: On the attribution of black and brown carbon light absorption
796 using the Ångström exponent, Atmospheric Chemistry and Physics, 13, 10535-10543,
797 10.5194/acp-13-10535-2013, 2013.

798 Lai, S.-c., Zou, S.-c., Cao, J.-j., Lee, S.-c., and Ho, K.-f.: Characterizing ionic species in PM2.5
799 and PM10 in four Pearl River Delta cities, South China, Journal of Environmental Sciences, 19,
800 939-947, https://doi.org/10.1016/S1001-0742(07)60155-7, 2007.

801 Laskin, A., Laskin, J., and Nizkorodov, S. A.: Chemistry of atmospheric brown carbon,
802 Chemical reviews, 115, 4335-4382, 10.1021/cr5006167, 2015.

803 Lee, E., Chan, C. K., and Paatero, P.: Application of positive matrix factorization in source
804 apportionment of particulate pollutants in Hong Kong, Atmospheric Environment, 33, 3201-

805   3212, https://doi.org/10.1016/S1352-2310(99)00113-2, 1999.

806   Levine, J.: Biomass Burning Aerosols in a Savanna Region of the Ivory Coast, French Forum,
807   235-236, 1991.

808   Li, H., Han, Z., Cheng, T., Du, H., Kong, L., Chen, J., Zhang, R., and Wang, W.: Agricultural
809   Fire Impacts on the Air Quality of Shanghai during Summer Harvesttime, Aerosol and Air
810   Quality Research, 10.4209/aaqr.2009.08.0049, 2010.

811   Lin, P., Hu, M., Deng, Z., Slanina, J., Han, S., Kondo, Y., Takegawa, N., Miyazaki, Y., Zhao,
812   Y., and Sugimoto, N.: Seasonal and diurnal variations of organic carbon in PM2.5in Beijing
813   and the estimation of secondary organic carbon, Journal of Geophysical Research, 114,
814   10.1029/2008jd010902, 2009.

815   Liu, C., Chung, C. E., Yin, Y., and Schnaiter, M.: The absorption Ångström exponent of black
816   carbon: from numerical aspects, Atmospheric Chemistry and Physics, 18, 6259-6273,
817   10.5194/acp-18-6259-2018, 2018.

818   Liu, D., Taylor, J. W., Young, D. E., Flynn, M. J., Coe, H., and Allan, J. D.: The effect of
819   complex black carbon microphysics on the determination of the optical properties of brown
820   carbon, Geophysical Research Letters, 42, 613-619, 2015.

821   Liu, L., Mishchenko, M. I., and Patrick Arnott, W.: A study of radiative properties of fractal
822   soot aggregates using the superposition T-matrix method, Journal of Quantitative Spectroscopy
823   and Radiative Transfer, 109, 2656-2663, 10.1016/j.jqsrt.2008.05.001, 2008.

824   Ma, N., Zhao, C. S., Müller, T., Cheng, Y. F., Liu, P. F., Deng, Z. Z., Xu, W. Y., Ran, L., Nekat,
825   B., van Pinxteren, D., Gnauk, T., Müller, K., Herrmann, H., Yan, P., Zhou, X. J., and
826   Wiedensohler, A.: A new method to determine the mixing state of light absorbing carbonaceous
827   using the measured aerosol optical properties and number size distributions, Atmos. Chem.
828   Phys., 12, 2381-2397, 10.5194/acp-12-2381-2012, 2012.

829   Ma, Y., Li, S. Z., Zheng, J., Khalizov, A., Wang, X., Wang, Z., and Zhou, Y. Y.: Size-resolved
830   measurements of mixing state and cloud-nucleating ability of aerosols in Nanjing, China, J.
831   Geophys. Res.-Atmos., 122, 9430-9450, 10.1002/2017jd026583, 2017.

832   Mie, G.: Beitrage Zur Optik Truber Medien, Speziell Kolloidaler Metallosungen, Annalen Der
833   Physik, 25, 377, 1908.

834   Moosmüller, H., Chakrabarty, R. K., Ehlers, K. M., and Arnott, W. P.: Absorption Ångström
835   coefficient, brown carbon, and aerosols: basic concepts, bulk matter, and spherical particles,
836   Atmospheric Chemistry and Physics, 11, 1217-1225, 10.5194/acp-11-1217-2011, 2011.

837   Nakayama, T., Ikeda, Y., Sawada, Y., Setoguchi, Y., Ogawa, S., Kawana, K., Mochida, M.,
838   Ikemori, F., Matsumoto, K., and Matsumi, Y.: Properties of light‐absorbing aerosols in the
839   Nagoya urban area, Japan, in August 2011 and January 2012: Contributions of brown carbon
840   and lensing effect, Journal of Geophysical Research Atmospheres, 119, 12,721-712,739, 2015.

841 Olson, M. R., Victoria Garcia, M., Robinson, M. A., Van Rooy, P., Dietenberger, M. A., Bergin,
842 M., and Schauer, J. J.: Investigation of black and brown carbon multiple-wavelength-dependent
843 light absorption from biomass and fossil fuel combustion source emissions, Journal of
844 Geophysical Research: Atmospheres, 120, 6682-6697, 10.1002/2014jd022970, 2015.

845 Pio, C. A., Legrand, M., Alves, C. A., Oliveira, T., Afonso, J., Caseiro, A., Puxbaum, H.,
846 Sanchez-Ochoa, A., and Gelencsér, A.: Chemical composition of atmospheric aerosols during
847 the 2003 summer intense forest fire period, Atmospheric Environment, 42, 7530-7543, 2008.

848 Qin, Y. M., Tan, H. B., Li, Y. J., Li, Z. J., Schurman, M. I., Liu, L., Wu, C., and Chan, C. K.:
849 Chemical characteristics of brown carbon in atmospheric particles at a suburban site near
850 Guangzhou, China, Atmospheric Chemistry and Physics Discussions, 1-23, 10.5194/acp-2018-
851 730, 2018.

852 Redmond, H., and Thompson, J. E.: Evaluation of a quantitative structure-property relationship
853 (QSPR) for predicting mid-visible refractive index of secondary organic aerosol (SOA),
854 Physical chemistry chemical physics : PCCP, 13, 6872-6882, 10.1039/c0cp02270e, 2011.

855 Ricchiazzi, P., Yang, S., Gautier, C., and Sowle, D.: SBDART: A Research and Teaching
856 Software Tool for Plane-Parallel Radiative Transfer in the Earth's Atmosphere, Bulletin of the
857 American Meteorological Society, 79, 2101-2114, 10.1175/1520-
858 0477(1998)079<2101:Sarats>2.0.Co;2, 1998.

859 Roesch, A.: Use of Moderate-Resolution Imaging Spectroradiometer bidirectional reflectance
860 distribution function products to enhance simulated surface albedos, Journal of Geophysical
861 Research, 109, 10.1029/2004jd004552, 2004.

862 Sareen, N., Schwier, A. N., Shapiro, E. L., Mitroo, D., and McNeill, V. F.: Secondary organic
863 material formed by methylglyoxal in aqueous aerosol mimics, Atmospheric Chemistry and
864 Physics, 10, 997-1016, 10.5194/acp-10-997-2010, 2010.

865 Satish, R., Shamjad, P., Thamban, N., Tripathi, S., and Rastogi, N.: Temporal Characteristics of
866 Brown Carbon over the Central Indo-Gangetic Plain, Environ Sci Technol, 51, 6765-6772,
867 10.1021/acs.est.7b00734, 2017.

868 Scarnato, B. V., Nielsen, K., Vahidinia, S., and Richard, D.: Effect of Aggregation and Mixing
869 on optical properties of Black Carbon, 2013,

870 Schmid, O., Artaxo, P., Arnott, W. P., Chand, D., Gatti, L. V., Frank, G. P., Hoffer, A., Schnaiter,
871 M., and Andreae, M. O.: Spectral light absorption by ambient aerosols influenced by biomass
872 burning in the Amazon Basin. I: Comparison and field calibration of absorption measurement
873 techniques, Atmos. Chem. Phys., 6, 3443-3462, 10.5194/acp-6-3443-2006, 2006.

874 Segura, S., Estellés, V., Titos, G., Lyamani, H., Utrillas, M. P., Zotter, P., Prévôt, A. S. H.,
875 Močnik, G., Alados-Arboledas, L., and Martínez-Lozano, J. A.: Determination and analysis of
876 in situ spectral aerosol optical properties by a multi-instrumental approach, Atmospheric
877 Measurement Techniques, 7, 2373-2387, 10.5194/amt-7-2373-2014, 2014.

878   Seinfeld, J. H., and Pandis, S. N.: Atmospheric Chemistry and Physics, John Wiley & Sons, Inc,
879   New York, 1998.

880   Stokes, G. M., and Schwartz, S. E.: The Atmospheric Radiation Measurement (ARM) Program:
881   Programmatic Background and Design of the Cloud and Radiation Test Bed, Bulletin of the
882   American Meteorological Society, 75, 1201–1221, 1994.

883   T. C. Bond, †, M. Bussemer, B. Wehner, S. Keller, R. J. Charlson, a., and Heintzenberg‡, J.:
884   Light Absorption by Primary Particle Emissions from a Lignite Burning Plant, Environmental
885   Science & Technology, 33, 3887-3891, 1999.

886   Tan, H., Liu, L., Fan, S., Li, F., Yin, Y., Cai, M., and Chan, P. W.: Aerosol optical properties and
887   mixing state of black carbon in the Pearl River Delta, China, Atmos. Environ., 131, 196-208,
888   https://doi.org/10.1016/j.atmosenv.2016.02.003, 2016a.

889   Tan, H., Yin, Y., Li, F., Liu, X., Chan, P. W., Deng, T., Deng, X., Wan, Q., and Wu, D.:
890   Measurements of particle number size distributions and new particle formations events during
891   winter in the Pearl River Delta region, China, Journal of Tropical Meteorology, 22, 191-199,
892   10.16555/j.1006-8775.2016.02.009, 2016b.

893   Waldman, J. M., Lioy, P. J., Zelenka, M., Jing, L., Lin, Y. N., He, Q. C., Qian, Z. M., Chapman,
894   R., and Wilson, W. E.: Wintertime measurements of aerosol acidity and trace elements in
895   Wuhan, a city in central China, Atmospheric Environment. Part B. Urban Atmosphere, 25, 113-
896   120, https://doi.org/10.1016/0957-1272(91)90045-G, 1991.

897   Wang, J., Nie, W., Cheng, Y., Shen, Y., Chi, X., Wang, J., Huang, X., Xie, Y., Sun, P., Xu, Z.,
898   Qi, X., Su, H., and Ding, A.: Light absorption of brown carbon in eastern China based on 3-
899   year multi-wavelength aerosol optical property observations and an improved absorption
900   Ångström exponent segregation method, Atmospheric Chemistry and Physics, 18, 9061-9074,
901   10.5194/acp-18-9061-2018, 2018.

902   Washenfelder, R. A., Attwood, A. R., Brock, C. A., Guo, H., Xu, L., Weber, R. J., Ng, N. L.,
903   Allen, H. M., Ayres, B. R., and Baumann, K.: Biomass burning dominates brown carbon
904   absorption in the rural southeastern United States, Geophysical Research Letters, 42, 653-664,
905   2015.

906   Wex, H., Neusüß, C., Wendisch, M., Stratmann, F., Koziar, C., Keil, A., Wiedensohler, A., and
907   Ebert, M.: Particle scattering, backscattering, and absorption coefficients: An in situ closure
908   and sensitivity study, Journal of Geophysical Research Atmospheres, 107, LAC-1-LAC 4-18,
909   2002.

910   Wu, C., Wu, D., and Yu, J. Z.: Quantifying black carbon light absorption enhancement with
911   a novel statistical approach, Atmospheric Chemistry and Physics, 18, 289-309, 10.5194/acp-
912   18-289-2018, 2018.

913   Wu, C., Wu, D., and Yu, J.: Estimation and Uncertainty Analysis of Secondary Organic Carbon
914   Using One‐Year of Hourly Organic and Elemental Carbon Data, Journal of Geophysical

915   Research Atmospheres, 124, 2774-2795, 10.1029/2018JD029290, 2019.

916   Wu, D., Mao, J., Deng, X., Tie, X., Zhang, Y., Zeng, L., Li, F., Tan, H., Bi, X., Huang, X., Chen,
917   J., and Deng, T.: Black carbon aerosols and their radiative properties in the Pearl River Delta
918   region, Science in China Series D: Earth Sciences, 52, 1152-1163, 10.1007/s11430-009-0115-
919   y, 2009.

920   Xie, C., Xu, W., Wang, J., Wang, Q., Liu, D., Tang, G., Chen, P., Du, W., Zhao, J., Zhang, Y.,
921   Zhou, W., Han, T., Bian, Q., Li, J., Fu, P., Wang, Z., Ge, X., Allan, J., Coe, H., and Sun, Y.:
922   Vertical characterization of aerosol optical properties and brown carbon in winter in urban
923   Beijing, China, Atmospheric Chemistry and Physics Discussions, 1-28, 10.5194/acp-2018-788,
924   2018.

925   Yu, J., Yan, C., Liu, Y., Li, X., Zhou, T., and Zheng, M.: Potassium: A Tracer for Biomass
926   Burning   in   Beijing?,   Aerosol   and   Air   Quality   Research,   18,   2447-2459,
927   10.4209/aaqr.2017.11.0536, 2018.

928   Yuan, J. F., Huang, X. F., Cao, L. M., Cui, J., Zhu, Q., Huang, C. N., Lan, Z. J., and He, L. Y.:
929   Light absorption of brown carbon aerosol in the PRD region of China, Atmospheric Chemistry
930   and Physics, 16, 1433-1443, 10.5194/acp-16-1433-2016, 2016.

931   Zhang, Y., Li, Z., Sun, Y., Lv, Y., and Xie, Y.: Estimation of atmospheric columnar organic
932   matter (OM) mass concentration from remote sensing measurements of aerosol spectral
933   refractive indices, Atmospheric Environment, 179, 107-117, 10.1016/j.atmosenv.2018.02.010,
934   2018.

935   Zhou, S., Wang, T., Wang, Z., Li, W., Xu, Z., Wang, X., Yuan, C., Poon, C. N., Louie, P. K. K.,
936   Luk, C. W. Y., and Wang, W.: Photochemical evolution of organic aerosols observed in urban
937   plumes from Hong Kong and the Pearl River Delta of China, Atmospheric Environment, 88,
938   219-229, 10.1016/j.atmosenv.2014.01.032, 2014.
939
940

Table 1. Inter-comparison of the performance of various Mie-calculation schemes. The base case is based on the empirical distribution function and mixing states of BC particles obtained from previous field measurements at the same site. $\Phi_{N,CV}$ denotes the portion of non-BC particles and r_{ext} is the mass portion of externally mixed BC with respect to total BC. AAE_{BC} is the absorption Ångström exponent of BC, and the subscript represents the wavelength range. $Abs_{BrC,370}\%$ and $Abs_{BrC,520}\%$ are the BrC absorption contributions at 370 nm and 520 nm, respectively. $Calcabs_{880}$ is the calculated absorption at 880 nm using Mie model. $Measabs_{880}$ is the measured absorption by an Aethalometer at 880 nm. b is the intercept of the regression analysis between $Measabs_{880}$ and $Calcabs_{880}$, i.e., $Calcabs_{880}=b*\,Measabs_{880}$. R^2 is the correlation coefficient of the equation. The refractive index of BC core ($\widetilde{m}_{core}$) and nonlight-absorbing particles ($\widetilde{m}_{non}$) is set to be 1.80-0.54i and 1.55-10^{-7}i, respectively (Tan et al., 2016a),

Case #	Scheme	$\Phi_{N,CV}$	r_{ext}	AAE BC,370-520	AAE BC,520-880	Abs BrC,370%	Abs BrC,520%	Calc abs880	Meas abs880	b	R^2
Base		0.384 to 0.137	0.58	0.723	0.962	34.13%	15.96%	21.869		1.019	0.979
1		0	1	0.331	0.626	51.64%	29.57%	15.832		0.747	0.968
2		0	0	0.856	1.128	24.76%	8.28%	27.827		1.295	0.976
3		0	0.58	0.745	0.974	33.22%	15.46%	21.936	**21.199**	1.029	0.979
4		0.384 to 0.137	0	0.835	1.111	26.01%	9.14%	27.302		1.269	0.975
5		0.5	0	0.778	1.043	29.96%	12.30%	24.921		1.150	0.968
6		0.5	0.58	0.674	0.928	36.39%	17.49%	20.897		0.977	0.975

954 **Table 2.** Observational studies of the BrC light absorption coefficient and contribution in the

955 near-ultraviolet wavelength range in East Asia.

Periods	Location	λ (nm)	Mean BrC absorption coefficient	Mean BrC absorption contribution	Instrumentation	Reference
Nov. 2014 – Jan. 2015	Guangzhou (China)	370	17.6 Mm^{-1} 23.5 Mm^{-1}	26.2% (AAE$_{BC}$=1) 34.1% (corrected)	Aethalometer AE-33	This study
Jan. 2014 – Feb. 2014; Sep. 2014 – Oct. 2014	Shenzhen (China)	405	3.0 Mm^{-1} 1.4 Mm^{-1}	11.7% (winter) 6.3% (fall)	PASS-3	Yuan et al. (2016)
Nov. 2014	Heshan (China)	405	3.9 Mm^{-1}	12.1%	PASS-3	Yuan et al. (2016)
Nov. 2016– Dec. 2016	Beijing (China)	370	106.4 Mm^{-1} 93.8 Mm^{-1}	46% (at the ground) 48% (at 260 m)	Aethalometer AE-33	Xie et al. (2018)
Jun. 2013 – May. 2016	Nanjing (China)	370	35.8 Mm^{-1}	16.7%	Aethalometer AE-31	Wang et al. (2018)
Jan. 2012	Nagoya (Japan)	405	Not detected	11% (300°C) 17% (400°C)	Thermodenuder PASS-3	Nakayama et al. (2015)

956
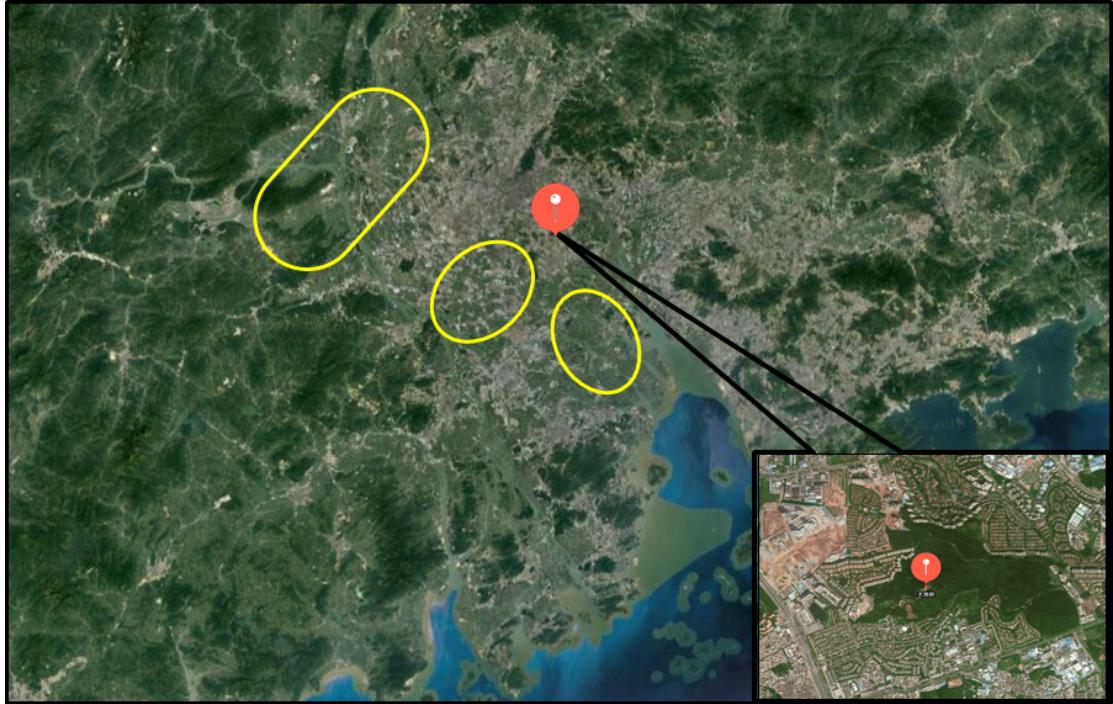
957
958 Figure 1. The location of Panyu station (CAWNET) in the PRD region (indicated by the red

959 dot). The plain areas within the yellow circles are the main rural areas of western PRD.

960

961

962
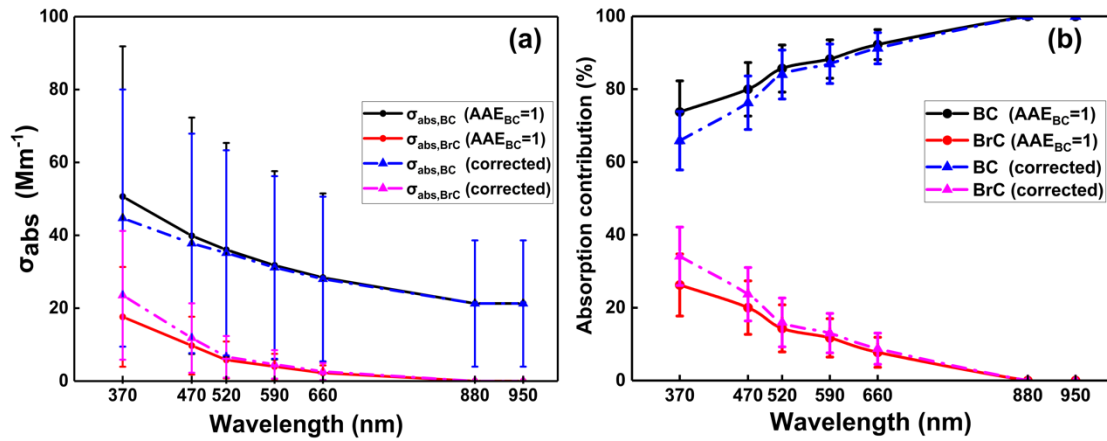
Figure 2. (a) BC and BrC particle average light absorption coefficients at different wavelengths under different AAE_{BC} assumptions; the whiskers represent an error of one standard deviation. (b) Contributions of BC and BrC to the total light absorption coefficient at different wavelengths under different AAE_{BC} assumptions; the whiskers represent an error of one standard deviation.

968
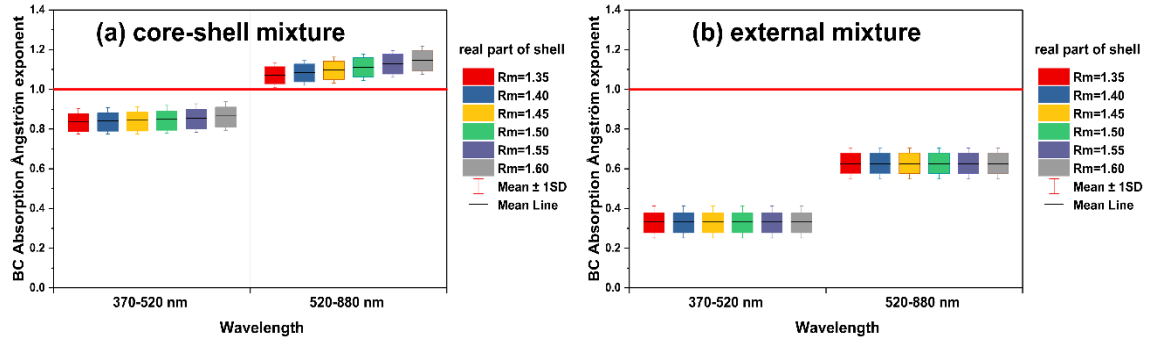
Figure 3. Influence of the wavelength-independent refractive index of the non-absorbing materials on the (a) AAEs of the core-shell mixture and (b) AAEs of the external mixture with a constant BC core refractive index ($\tilde{m}_{core}=1.80\text{-}0.54i$). The imaginary part of the non(less)-absorbing shell was set to 10^{-7}, while the real part varied from 1.35 to1.60. In each panel, the boundaries of the box represent the 75th and 25th percentiles; the whiskers above and below each box indicate an error of one standard deviation; the black lines in the boxes denote the average values. In panels a and b, the red line indicates where $AAE_{BC}=1$.
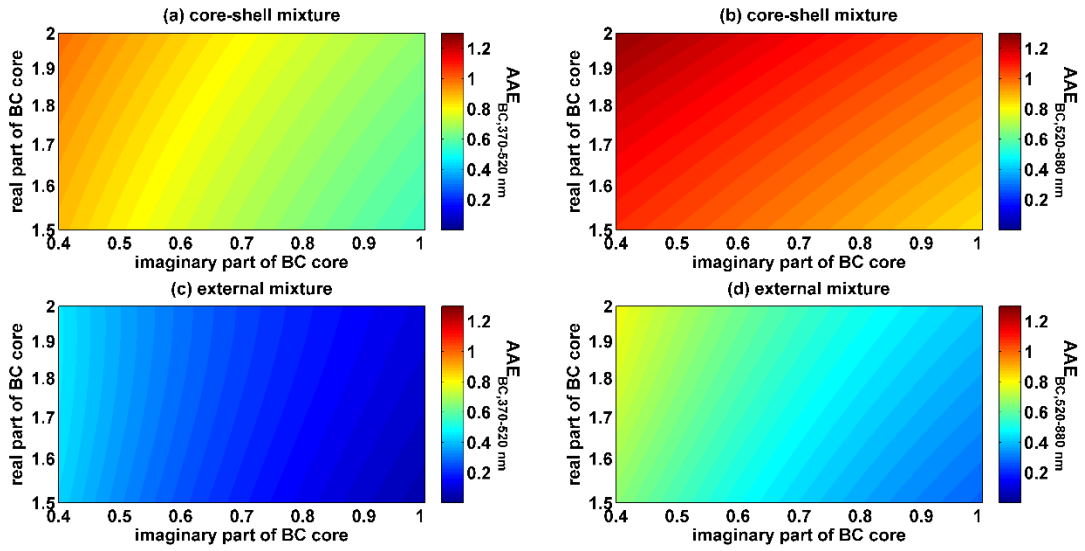
979 Figure 4. Influence of the wavelength-independent refractive index of the BC core on AAEs

980 with a constant shell refractive index ($\widetilde{m}_{shell}$=*1.55-10^{-7}i*). A core-shell mixture was used for

981 panels a and b, and an external mixture was used for panels c and d. The real part of $\widetilde{m}_{core}$

982 varied from 1.5 to 2.0, with a step of 0.05, and the imaginary part of $\widetilde{m}_{core}$ varied from 0.4 to

983 1.0, with a step of 0.05.

984
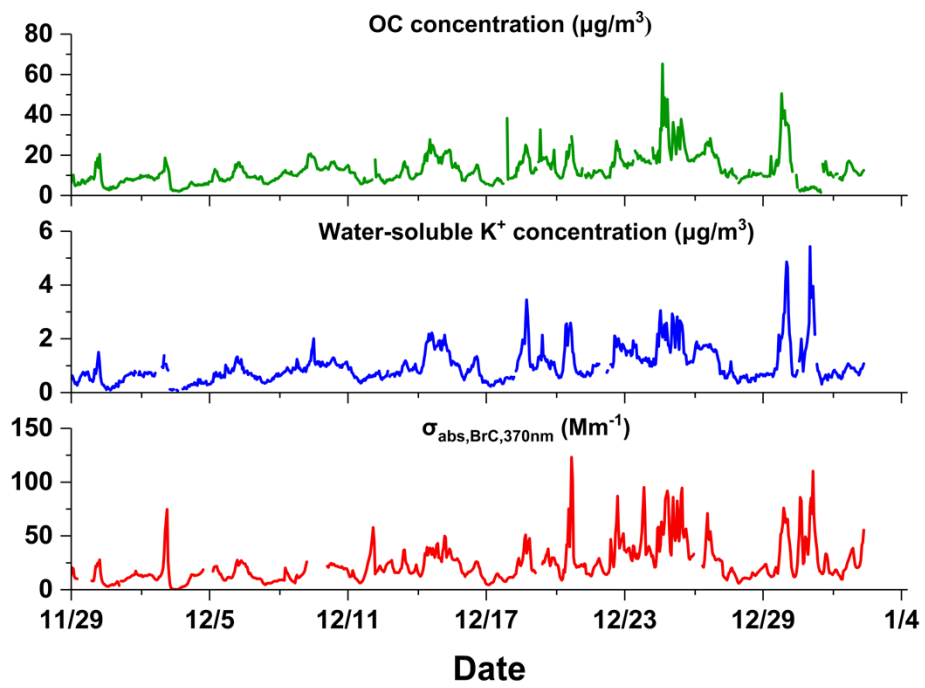
985

986 Figure 5. Time series of the OC aerosol mass concentration (green line), water-soluble K$^+$ mass

987 concentration (blue line), and BrC light absorption (red line).

988

989

(a) OC concentration (µg/m³)   (b) K⁺ concentration (µg/m³)   (c) $\sigma_{abs,\,BrC,\,370nm}$ (Mm⁻¹)
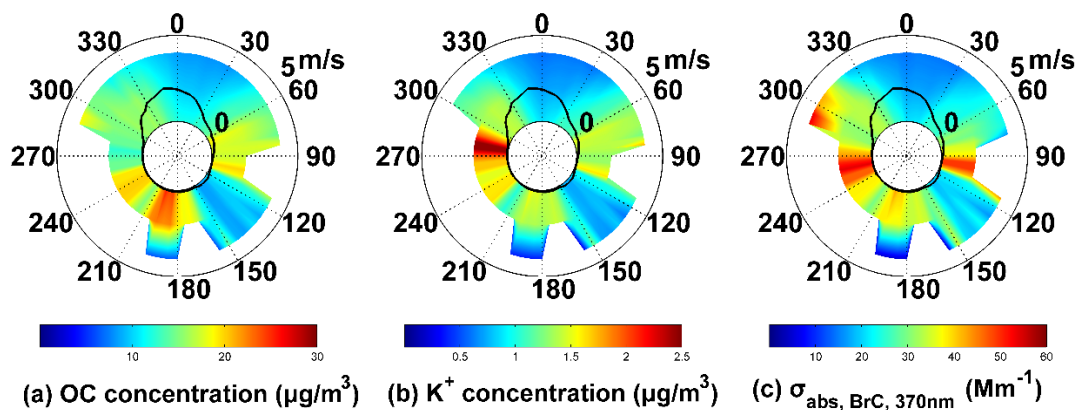
990

991   Figure 6. Wind rose plots of OC (a), K⁺ (b), and $\sigma_{abs,BrC,370nm}$ (c). In each panel, the black solid

992   lines denote the frequency of the wind direction. The shaded contour represents the average

993   values of the corresponding species for that wind speed (radial length) and wind direction

994   (transverse direction) in polar coordinates.

995

996
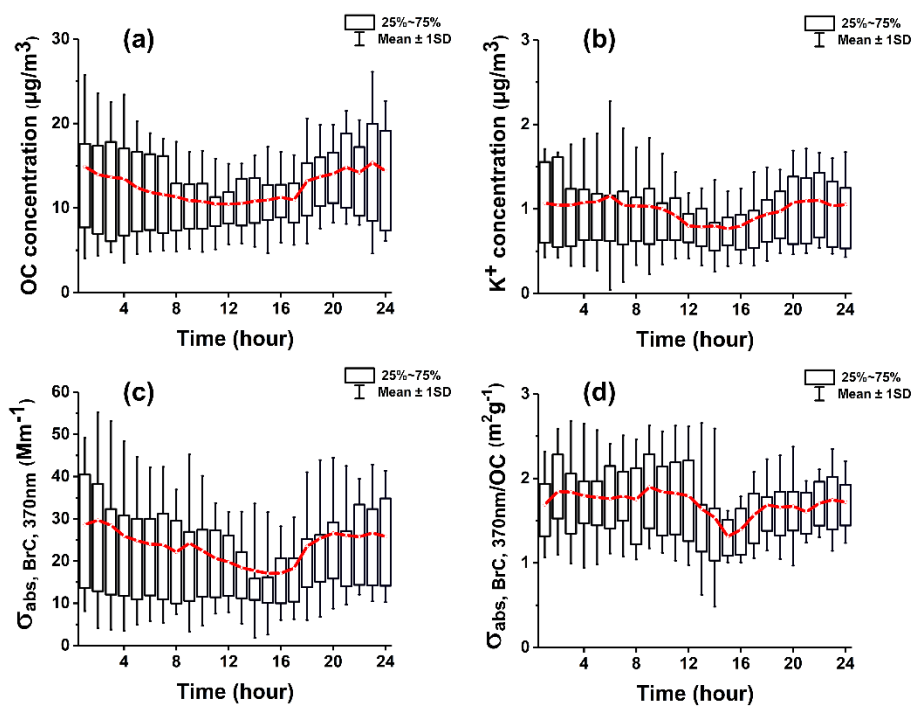
997

998   Figure 7. Box-whisker plots of diurnal trends in the OC concentration (a), water-soluble K+

999   concentration (b), $\sigma_{abs,BrC,370nm}$ (c), and $\sigma_{abs,BrC,370nm}$ /OC (d). The red traces represent the

1000   variation in the average value. The upper and lower boundaries of the box represent the 75th

1001   and 25th percentiles, respectively; the whiskers above and below each box represent an error

1002   of one standard deviation.

1003
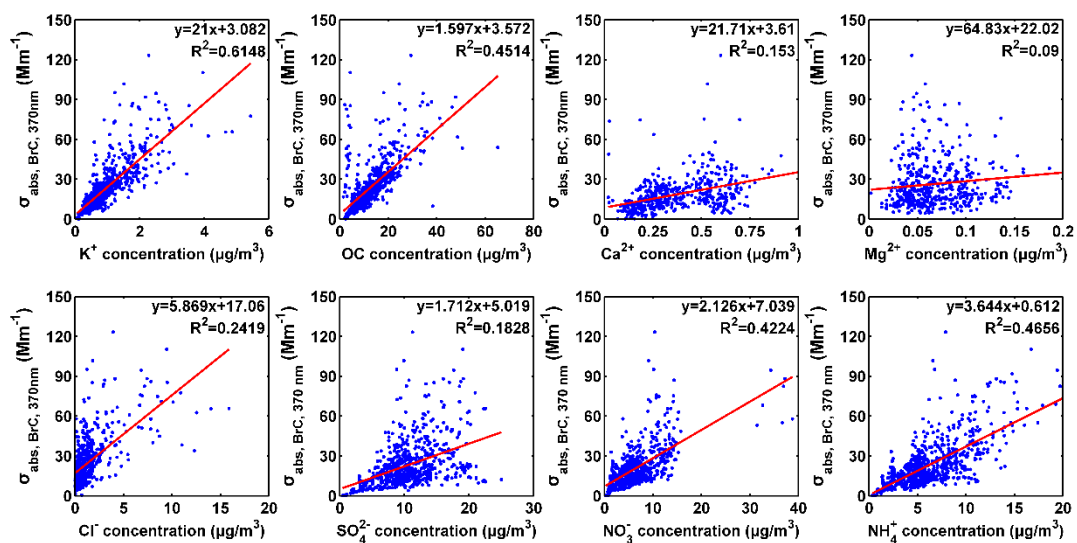
1004

1005   Figure 8. Correlations of the BrC absorption coefficient at 370 nm with OC, water-soluble K^+,

1006 Ca^{2+}, Mg^{2+}, Cl^-, SO_4^{2-}, NO_3^-, and NH_4^+ aerosol concentrations.
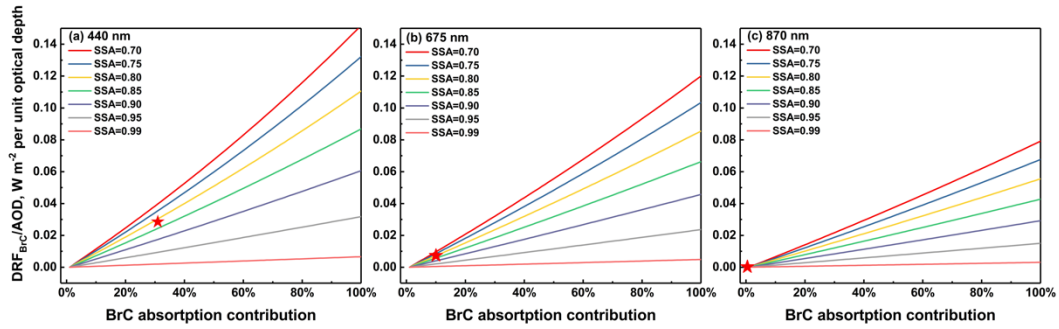
1007

1008 Figure 9. BrC radiative forcing efficiencies, which are defined as the BrC TOA direct radiative

1009 forcing divided by the AOD, as a function of the BrC to BC absorption ratio and *SSA* measured

1010 at the surface. The average AOD of the three wavelengths, the average ASY of the three

1011 wavelengths, a solar zenith angle of 55°, and average shortwave broadband surface albedo were

1012 used in the calculation. The red star corresponds to the average *SSA* and BrC absorption

1013 contributions determined from this campaign.